

# Robust and Safe N-Spacecraft Swarming in Perturbed Near-Circular Orbits

By Adam W. KOENIG,<sup>1)</sup> Simone D'AMICO,<sup>1)</sup>

<sup>1)</sup>Department of Aeronautics and Astronautics, Stanford University, Stanford, California, USA

This paper presents a new guidance and control methodology for spacecraft swarms based on relative orbital elements. In contrast to literature that relies on complex and computationally expensive algorithms designed for robotic systems, this paper generalizes flight-proven techniques used for guidance and control of binary formations to accommodate a large number of spacecraft. In particular, the formation design problem is cast in the relative orbital elements to allow derivation of linear constraints that ensure passively bounded relative motion in perturbed near-circular orbits. This approach also enables derivation of constraints that ensure collision avoidance including uncertainty at a computational cost that scales only linearly with the number of spacecraft. Additionally, two swarm formations are identified that ensure a passive minimum separation between all spacecraft in either the orbit plane or the plane perpendicular to the flight direction. To counteract the effects of differential drag, a set of nonlinear state space control laws is developed that requires actuation in only the (anti-)flight direction, which can be realized using low-thrust or differential drag control. These control laws are employed in a hybrid passive/active control architecture that only actuates the spacecraft when necessary to ensure collision avoidance, allowing periodic passive drifts of up to several days. The proposed formation designs and control architectures are validated in simulations of a reference mission scenario using a high-fidelity numerical orbit propagator. It is demonstrated that the proposed swarm formations provide safe and bounded relative motion between at least tens of spacecraft for weeks or longer subject to multiple perturbations at minimum actuation and computation cost.

**Key Words:** spacecraft swarms, formation design, relative dynamics, guidance, control

## Nomenclature

$A$	: cross-sectional area of spacecraft	$\delta$	: relative parameter between spacecraft
$a$	: orbit semimajor axis	$\delta\alpha$	: relative orbital elements
$B$	: ballistic coefficient	$\delta a$	: relative semimajor axis
$C_D$	: drag coefficient	$\delta e$	: relative eccentricity vector
$D$	: differential drag control authority	$\delta i$	: relative inclination vector
$e$	: orbit eccentricity	$\delta\lambda$	: relative mean longitude
$I$	: spacecraft moment of inertia	$\epsilon$	: minimum safe separation
$i$	: orbit inclination	$\zeta$	: control parameter for $\delta e$
$J_2$	: second order zonal geopotential harmonic	$\eta$	: speed parameter for attitude controller
$M$	: orbit mean anomaly	$\theta$	: phase angle of $\delta e$
$m$	: spacecraft mass	$\kappa$	: orbit-specific $J_2$ parameter
$N$	: number of deputies in swarm	$\Lambda$	: nonlinear control switching line
$n$	: orbit mean motion	$\mu$	: earth gravitational constant
$P$	: applied torque	$\rho$	: local atmospheric density
$p$	: perturbing acceleration	$\bar{\rho}$	: averaged atmospheric density over one orbit
$R_E$	: radius of the earth	$\sigma$	: uncertainty parameter
$t$	: time	$\tau$	: propagation time
$U$	: instantaneous acceleration due to thrust	$\Phi$	: state transition matrix (STM)
$U^*$	: maximum allowed time-averaged $U$	$\varphi$	: phase angle of $\delta i$
$u$	: orbit mean argument of latitude	$\Omega$	: orbit right ascension of the ascending node
$v$	: spacecraft velocity	$\omega$	: orbit argument of perigee
$W, X, Y, Z$	: integer spacing parameters	$\dot{\omega}$	: precession rate of $\omega$ due to $J_2$
$\mathbf{x}$	: absolute position and velocity	<b>Superscripts &amp; Subscripts</b>	
$\alpha$	: Keplerian orbit elements	$c$	: chief spacecraft
$\beta$	: attitude of spacecraft	$com$	: control command
$\Gamma$	: control input matrix	$d$	: deputy spacecraft
$\Delta B$	: differential ballistic coefficient	$db$	: deadband parameter
$\Delta B^*$	: maximum allowed time-averaged $\Delta B$	$drag$	: atmospheric drag parameter
$\Delta B_{max}$	: maximum achievable instantaneous $\Delta B$	$drift$	: free drift phase parameter
$\Delta t$	: change in time	$err$	: error with respect to guidance profile
		$j, k$	: deputy identifiers, $j, k \leq z$

<i>man</i>	:	maneuver parameter
<i>rec</i>	:	reconfiguration parameter
<i>sep</i>	:	nominal separation parameter
<i>N</i>	:	cross-track direction
<i>R</i>	:	radial direction
<i>T</i>	:	along-track direction

## 1. Introduction

Spacecraft formation flying has become an area of great interest to the scientific community in recent years following the success of missions such as GRACE (NASA),<sup>1)</sup> TanDEM-X (DLR),<sup>2)</sup> MMS (NASA)<sup>3)</sup> and others. These missions have demonstrated capabilities in earth and space science that would be difficult or impossible to achieve using a single monolithic spacecraft. Additionally, use of a spacecraft formation adds a degree of fault tolerance to mission designs. Specifically, a spacecraft formation may be able to compensate for the failure of a single spacecraft by distributing the workload among the remaining vehicles. In contrast, a major malfunction on a monolithic spacecraft would almost certainly result in mission failure. At present, the guidance, navigation, and control (GN&C) problem for binary spacecraft formations is well-studied in literature.<sup>4–12)</sup>

The success of these missions has also prompted interest in formations consisting of a large number of small, low-cost spacecraft. These so-called spacecraft swarms could enable new missions that require massively distributed sensing capabilities such as distributed antennas or sparse aperture arrays. Additionally, spacecraft swarms could perform in-space assembly of large structures. In order to be cost-effective as compared to a monolithic spacecraft or a smaller formation, the spacecraft in a swarm must be both smaller and cheaper. As a result, the spacecraft will have limited sensing, actuation, and computation capabilities. Also, ensuring collision avoidance is especially challenging for swarms due to the large number of spacecraft. To date, most GN&C studies for multi-agent systems have been conducted in the context of robotic applications.<sup>13–17)</sup> These studies make one or more of three assumptions that limit their applicability to spacecraft swarms: 1) a simple dynamic model, 2) high control authority, or 3) ample computational resources. At present, there is little literature on multi-agent systems that addresses both the complex dynamics of the space environment and the computation, sensing, and actuation limitations of small spacecraft.<sup>18–24)</sup> Of these studies, the Silicon Wafer Integrated Femtosatellites (SWIFT) project from the Jet Propulsion Laboratory<sup>20)</sup> is one of the most promising. This proposal calls for hundreds to thousands of 100 gram spacecraft that are distributed along a set of concentric passive relative orbits that satisfy a set of nonlinear  $J_2$  energy matching conditions to achieve bounded relative motion and collision avoidance.<sup>22)</sup> However, this design is still subject to significant limitations. First, frequent maneuvers are required to counteract the effects of differential drag. Second, the proposed guidance and control algorithms call for computationally expensive techniques such as distributed auction algorithms and sequential convex programming.<sup>21,23,24)</sup> Finally, the control algorithms call for full 6-DoF control of all spacecraft in the swarm, requiring costly actuators

that are not readily available for small spacecraft.

With these limitations in mind, this paper presents a new guidance and control methodology for spacecraft swarms based on relative orbital elements (ROE). This methodology generalizes techniques used to design and control binary formations to accommodate a large number of spacecraft. These techniques have extensive flight heritage on missions including GRACE,<sup>25)</sup> TanDEM-X,<sup>26)</sup> PRISMA,<sup>27)</sup> and others. Within this context, this paper makes five contributions to the state-of-the-art. First, it is demonstrated that a sufficient condition to ensure passively bounded relative motion in  $J_2$ -perturbed near-circular orbits is that all spacecraft in the swarm have the same semimajor axis and inclination. This requirement is formulated as a pair of linear constraints in the ROE state space as opposed to the complex nonlinear  $J_2$  energy matching conditions derived by Morgan for a relative state based on Cartesian position and velocity.<sup>22)</sup> Second, two swarm formations are identified that simultaneously satisfy these constraints and ensure a passive minimum separation between all spacecraft in either the orbit plane or the plane perpendicular to the flight direction. The latter formation effectively generalizes D’Amico’s eccentricity/inclination ( $e/i$ ) vector separation concept<sup>6)</sup> to an arbitrary number of spacecraft. Additionally, this formation ensures passive collision avoidance for periods of days or longer subject to both  $J_2$  and differential drag. Third, a set of analytical constraints is derived for each of these swarm formations that ensures collision avoidance including uncertainty. The computational cost of verifying that these constraints are satisfied varies linearly with the number of spacecraft instead of quadratically as previously suggested in literature.<sup>22)</sup> Fourth, nonlinear state space control laws are derived that counteract the effects of differential drag to ensure long-term collision avoidance and bounded relative motion using an approach inspired by recently derived closed-form minimum-cost impulsive maneuver sequences.<sup>28,29)</sup> In particular, efficient control of the in-plane ROE is achieved using actuation in only the (anti-)flight direction, which can be realized using either low-thrust or differential drag control. For the swarm formation using  $e/i$  vector separation, these control laws are employed in a hybrid passive/active architecture which periodically allows the swarm to freely drift and only commands maneuvers when necessary to ensure collision avoidance or prevent the inter-spacecraft separation from exceeding user-defined limits. Finally, the formation designs and control architectures are validated through simulations using a high-fidelity orbit propagator including all relevant perturbations in low earth orbit (LEO). These simulations demonstrate that the proposed swarm designs are able to allow at least tens of spacecraft to safely operate in close proximity at minimal actuation and computation cost.

After this introduction, the required conditions to ensure passively bounded relative motion and collision avoidance for a binary spacecraft formation in LEO are reviewed in Sec. 2. In Sec. 3, these techniques are generalized to spacecraft swarms. Sufficient constraints to ensure passive collision avoidance between all spacecraft including uncertainty at low computational cost are also derived. Control laws that counteract the effects of differential drag are developed in Sec. 4 for both low-thrust and differential drag control. Additionally, a hybrid passive/active

architecture is proposed that allows the swarm to freely drift when the minimum separation perpendicular to the flight direction between any two spacecraft is above a specified threshold. The simulated mission scenario used to validate the formation designs and control laws is presented in Sec. 5 and the results of the simulations are described in Sec. 6.

## 2. Background: Review of Binary Formation Design

The primary objective of this paper is to generalize the ROE-based techniques used to design and control binary formations to accommodate a large number of spacecraft. The ROE are a slowly-varying state whose components are defined as explicit functions of the Keplerian orbit elements. ROE-based state definitions offer numerous advantages over states defined from the relative position and velocity of the spacecraft including 1) simple and accurate dynamics models including multiple perturbations in arbitrarily eccentric orbits,<sup>30,31</sup> 2) closed-form fuel-optimal impulsive reconfiguration schemes,<sup>28,29</sup> and 3) analytical guarantees of long-term collision avoidance.<sup>6</sup> In particular, this paper adopts the quasi-nonsingular ROE defined by D'Amico,<sup>5</sup> which are given by

$$\delta\alpha = \begin{pmatrix} \delta a \\ \delta\lambda \\ \delta\mathbf{e} \\ \delta\mathbf{i} \end{pmatrix} = \begin{pmatrix} \delta a \\ \delta\lambda \\ \delta e_x \\ \delta e_y \\ \delta i_x \\ \delta i_y \end{pmatrix} = \begin{pmatrix} \delta a \\ \delta\lambda \\ \delta e \cos(\theta) \\ \delta e \sin(\theta) \\ \delta i \cos(\varphi) \\ \delta i \sin(\varphi) \end{pmatrix} = \begin{pmatrix} (a_d - a_c)/a_c \\ (M_d - M_c) + (\omega_d - \omega_c) + \cos(i_c)(\Omega_d - \Omega_c) \\ e_d \cos(\omega_d) - e_c \cos(\omega_c) \\ e_d \sin(\omega_d) - e_c \sin(\omega_c) \\ i_d - i_c \\ \sin(i_c)(\Omega_d - \Omega_c) \end{pmatrix} \quad (1)$$

where  $a$ ,  $e$ ,  $i$ ,  $\Omega$ ,  $\omega$ , and  $M$  are the Keplerian orbit elements. The orbit elements of the chief spacecraft are denoted by the subscript  $c$  and those of the deputy are denoted by the subscript  $d$ .

Spacecraft formations are generally designed to satisfy two key constraints: 1) the passive relative motion should be bounded, and 2) the spacecraft must not collide. A set of constraints on the ROE that satisfies both of these constraints is presented in the following.

### 2.1. Bounded Relative Motion

A key advantage of the ROE state is that the effects of perturbations manifest as secular and long-period effects in a subset of the state components. This property has enabled derivation of accurate linear dynamics models that include the effects of multiple perturbations.<sup>30-32</sup> These models include only the long-period and secular effects of the perturbations and neglect short-period oscillations to propagate a mean ROE state. For spacecraft formations in LEO, the dominant perturbations are  $J_2$  and differential atmospheric drag. The effects of these perturbations on formations in near-circular orbits are captured in a state transition matrix (STM) developed by Koenig,<sup>31</sup> which is briefly described in the following. Using an STM, the state at an arbitrary time is related to the state at time  $t$  by

$$\delta\alpha(t + \tau) = \Phi(\alpha_c(t), \tau)\delta\alpha(t) \quad (2)$$

where the STM  $\Phi$  is given as an explicit function of the absolute orbit of the chief  $\alpha_c$  at time  $t$  and the propagation time  $\tau$ . An STM that includes the secular effects of  $J_2$  on the ROE in near-circular orbits is obtained by neglecting all terms that are proportional to the eccentricity in the Koenig STM. The result is given by

$$\Phi^{J_2}(\alpha_c(t), \tau) = \begin{pmatrix} 1 & 0 & 0 & 0 & 0 & 0 \\ \Phi_{21}^{J_2} & 1 & 0 & 0 & \Phi_{25}^{J_2} & 0 \\ 0 & 0 & \cos(\dot{\omega}_c\tau) & -\sin(\dot{\omega}_c\tau) & 0 & 0 \\ 0 & 0 & \sin(\dot{\omega}_c\tau) & \cos(\dot{\omega}_c\tau) & 0 & 0 \\ 0 & 0 & 0 & 0 & 1 & 0 \\ \Phi_{61}^{J_2} & 0 & 0 & 0 & \Phi_{65}^{J_2} & 1 \end{pmatrix} \quad (3)$$

where the following substitutions are used for clarity

$$\eta_c = \sqrt{1 - e_c^2} \quad \kappa_c = \frac{3 J_2 R_E^2 \sqrt{\mu}}{4 a_c^{7/2} \eta_c^4} \\ \dot{\omega}_c = \kappa_c(5 \cos^2(i_c) - 1) \\ \Phi_{21}^{J_2} = -\left(\frac{3}{2}n_c + \frac{7}{2}\kappa_c(1 + \eta_c)(3 \cos^2(i_c) - 1)\right)\tau \quad (4) \\ \Phi_{25}^{J_2} = -\kappa_c(4 + 3\eta_c) \sin(2i_c)\tau \\ \Phi_{61}^{J_2} = \frac{7}{2}\kappa_c \sin(2i_c)\tau \quad \Phi_{65}^{J_2} = 2\kappa_c \sin^2(i_c)\tau$$

and  $n_c$  is the mean motion of the chief. It is clear that  $J_2$  produces three modes of relative motion in ROE space: 1) a constant drift of  $\delta\lambda$  (see 2nd row of STM), 2) a constant drift of  $\delta i_y$  (see 6th row of STM), and 3) a rotation of the relative eccentricity vector (see center terms of STM). Since the rotation of  $\delta\mathbf{e}$  is bounded, the necessary and sufficient conditions to ensure bounded relative motion are that the drift rates of  $\delta\lambda$  and  $\delta i_y$  must be zero. For inclined orbits, these conditions are met when  $\delta a = 0$  and  $\delta i_x = 0$ . For near-equatorial orbits, the constraint on  $\delta i_x$  can be relaxed because  $\Phi_{25}^{J_2}$  and  $\Phi_{65}^{J_2}$  are both small. The most significant consequence of these constraints is that all relative orbits with passively bounded relative motion under the effects of  $J_2$  exist in the four dimensional space spanned by  $\delta\lambda$ ,  $\delta e_x$ ,  $\delta e_y$ , and  $\delta i_y$ . Additionally, these linear constraints are much simpler than the nonlinear  $J_2$  energy matching conditions developed by Morgan for a relative state based on Cartesian position and velocity.<sup>22</sup>

Next, consider the differential drag perturbation. The effects of differential drag are included in the STM by augmenting the ROE with the drift rates of the relative semimajor axis and relative eccentricity vector due to differential drag, which can be estimated in flight. Using this approach, the evolution of the state including the  $J_2$  and differential drag perturbations is given by

$$\begin{pmatrix} \delta\alpha \\ \delta\dot{a}_{drag} \\ \delta\dot{\mathbf{e}}_{drag} \end{pmatrix}(t + \tau) = \Phi^{J_2+drag}(\alpha_c(t), \tau) \begin{pmatrix} \delta\alpha \\ \delta\dot{a}_{drag} \\ \delta\dot{\mathbf{e}}_{drag} \end{pmatrix}(t) \quad (5)$$

where  $\delta\dot{a}_{drag}$  and  $\delta\dot{\mathbf{e}}_{drag}$  are the time derivatives of the ROE due

to differential drag. The STM is given by

$$\Phi^{J_2+drag}(\alpha_c(t), \tau) = \begin{array}{c} \left[ \begin{array}{ccc|ccc} & \tau & 0 & 0 & & \\ & \Phi_{27}^{J_2+drag} & 0 & 0 & & \\ \Phi^{J_2}(\alpha_c(t), \tau) & 0 & \tau & 0 & & \\ & 0 & 0 & \tau & & \\ & 0 & 0 & 0 & & \\ & \Phi_{67}^{J_2+drag} & 0 & 0 & & \\ \hline \mathbf{0}^{3 \times 6} & & & & \mathbf{I}^{3 \times 3} & \end{array} \right] \end{array} \quad (6)$$

and the terms  $\Phi_{27}^{J_2+drag}$  and  $\Phi_{67}^{J_2+drag}$  are given by

$$\begin{aligned} \Phi_{27}^{J_2+drag} &= -\left(\frac{3}{4}n_c + \frac{7}{4}\kappa_c(1 + \eta_c)(3 \cos^2(i_c) - 1)\right)\tau^2 \\ \Phi_{67}^{J_2+drag} &= \frac{7}{4}\kappa_c \sin(2i_c)\tau^2 \end{aligned} \quad (7)$$

Even without explicit formulations of the time derivatives, this STM provides insight into the effects of differential drag that can be used to inform the formation design. First, the terms of the STM that govern the effects of differential drag are linear or quadratic in all of the in-plane ROE ( $\delta a$ ,  $\delta \lambda$ , and  $\delta e$ ). It follows that periodic maneuvers will be required to bound the in-plane ROE unless differential drag is negligible. Additionally, it is known that the mean motion is on the order of  $10^{-3}$  and  $\kappa_c$  is on the order of  $10^{-7}$  for spacecraft in LEO. It follows that the quadratic coupling between differential drag and Keplerian relative motion can produce large changes in  $\delta \lambda$  on the time scale of days even when  $\delta \dot{a}_{drag}$  is small. On the other hand, the terms defining the quadratic coupling between differential drag and  $J_2$  are small and can reasonably be neglected in the control design. This hypothesis will be validated by the simulation results presented in Sec. 6.

## 2.2. Collision Avoidance

It is now necessary to identify constraints on the ROE to ensure that the spacecraft do not collide. For near-circular orbits, the ROE are equivalent to the invariants of the Hill-Clohessey-Wiltshire equations to first order.<sup>33)</sup> The relationship between the ROE and the relative position  $\delta r$  and relative velocity  $\delta v$  is given by

$$\begin{aligned} \begin{pmatrix} \delta r_R \\ \delta r_T \\ \delta v_R \\ \delta v_T \end{pmatrix} &= a_c \begin{bmatrix} 1 & 0 & -\cos(u_c) & -\sin(u_c) \\ 0 & 1 & 2 \sin(u_c) & -2 \cos(u_c) \\ 0 & 0 & n_c \sin(u_c) & -n_c \cos(u_c) \\ -\frac{3}{2}n_c & 0 & 2n_c \cos(u_c) & 2n_c \sin(u_c) \end{bmatrix} \begin{pmatrix} \delta a \\ \delta \lambda \\ \delta e_x \\ \delta e_y \end{pmatrix} \\ \begin{pmatrix} \delta r_N \\ \delta v_N \end{pmatrix} &= a_c \begin{bmatrix} \sin(u_c) & -\cos(u_c) \\ n_c \cos(u_c) & n_c \sin(u_c) \end{bmatrix} \begin{pmatrix} \delta i_x \\ \delta i_y \end{pmatrix} \end{aligned} \quad (8)$$

where  $u_c = M_c + \omega_c$  is the mean argument of latitude and the subscripts  $R$ ,  $T$ , and  $N$  denote components in the radial, along-track, and cross-track directions, respectively. The radial direction is aligned with the vector from the center of the earth to the chief spacecraft, the cross-track direction is aligned with the angular momentum vector of the chief orbit, and the along-track direction completes the right-handed triad. It should be noted that the relationship in Eq. (8) holds and is more accurate for cylindrical and curvilinear coordinates,<sup>34)</sup> but this paper uses a rectilinear relative position and velocity to simplify subsequent derivations. Collision avoidance is ensured if the relative position vector is no smaller than a specified safe minimum value

$\epsilon$  for all  $u_c$ . Additionally, it is well known that estimates of  $\delta \lambda$  are often characterized by large uncertainty due to navigation, control, and maneuver execution errors as well as the differential drag perturbation.<sup>5)</sup> To reduce the impact of this uncertainty on mission operations, D'Amico developed the e/i vector separation concept<sup>6)</sup> to guarantee a passive minimum separation of  $\epsilon$  perpendicular to the flight direction. If  $\delta a = 0$  to prevent the formation from drifting apart, the necessary and sufficient condition to ensure a minimum separation of  $\epsilon$  in the RN-plane is given by

$$\frac{\sqrt{2}|\delta e \cdot \delta i|}{(\delta e^2 + \delta i^2 + |\delta e + \delta i| \cdot |\delta e - \delta i|)^{1/2}} \geq \frac{\epsilon}{a_c} \quad (9)$$

This equation can be reformulated as

$$|\delta e \cdot \delta i| \geq \frac{\epsilon}{a_c} \sqrt{\delta e^2 + \delta i^2 - \frac{\epsilon^2}{a_c^2}} \quad (10)$$

Under the additional assumption that  $\delta i_x = 0$  to avoid drift due to  $J_2$ , this condition can be reduced to

$$\delta e_y^2 \geq \left(\frac{a_c^2 \delta i_y^2}{\epsilon^2} - 1\right)^{-1} \delta e_x^2 + \frac{\epsilon^2}{a_c^2} \quad (11)$$

provided that  $a_c \delta i_y \geq \epsilon$ . This constraint can also be formulated in polar coordinates as

$$|\cos(\theta)| \leq \frac{\epsilon}{a_c \delta i_y} \sqrt{\left(1 - \frac{\epsilon^2}{a_c^2 \delta e^2}\right) \left(\frac{a_c^2 \delta i_y^2}{\epsilon^2} - 1\right)} \quad (12)$$

which only has a real solution if  $a_c \delta e \geq \epsilon$ . The constraints in Eqs. (11) and (12) define a hyperbolic exclusion zone in ROE state space as illustrated in Figure 1. In this figure, the diag-

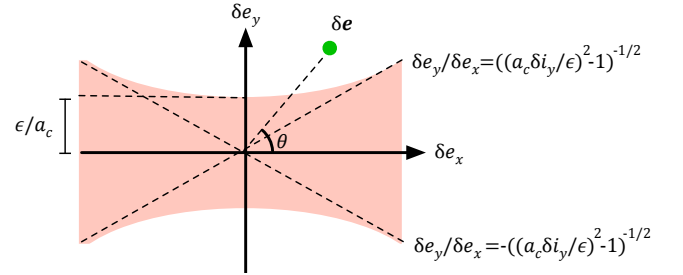


Fig. 1. Hyperbolic exclusion zone (red) for  $\delta e$  to ensure RN-plane separation when  $\delta i_x = 0$ .

onal dashed lines are the asymptotes of the hyperbola and the formation will have a minimum separation in the RN-plane of at least  $\epsilon$  if the relative eccentricity vector is outside the red region. Also, unless the formation is at the critical inclination ( $i_c \approx 63.4^\circ$  or  $116.6^\circ$ ), the relative eccentricity vector will rotate due to  $J_2$ . As a result, the minimum separation in the RN-plane will periodically decrease to zero when the relative eccentricity vector is horizontal. In order to ensure safe separation between the spacecraft without requiring maneuvers to counteract the rotation of  $\delta e$  due to  $J_2$ , it will be necessary to ensure that the spacecraft are separated in the RT-plane during these phases. The relationship between the relative motion in the RT-plane and the ROE is illustrated in Figure 2. In order to derive collision avoidance constraints, it is assumed that  $\delta a = 0$  to ensure

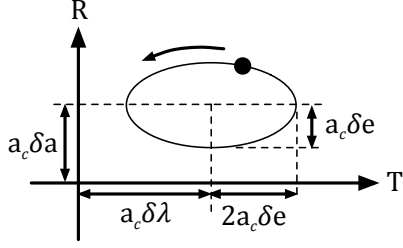


Fig. 2. Instantaneous relationship between in-plane ROE and relative motion. The the along-track drift of the ellipse due to nonzero  $\delta a$  is neglected for simplicity.

that the relative motion ellipse is stationary. Under this assumption, it is evident from Figure 2 that the spacecraft will have a minimum separation of  $\epsilon$  if

$$a_c |\delta \lambda| \geq 2a_c \delta e + \epsilon \quad (13)$$

However, the inter-spacecraft separation may have to be large to satisfy this constraint. Formations in which the deputy encircles the chief are of greater interest in the swarm design problem in order to allow operations in close proximity. Since the deputy traces out an ellipse with a two-by-one aspect ratio in the RT-plane, the constraint on  $\delta \lambda$  that ensures a safe minimum separation is given by

$$a_c |\delta \lambda| \leq f(a_c, \delta e, \epsilon) \quad (14)$$

$$f(a_c, \delta e, \epsilon) = \begin{cases} \sqrt{3(a_c^2 \delta e^2 - \epsilon^2)} & \text{if } \epsilon \leq a_c \delta e < 2\epsilon \\ 2a_c \delta e - \epsilon & \text{if } a_c \delta e \geq 2\epsilon \end{cases}$$

The limiting cases for each of the constraints in Eqs. (13) and (14) are illustrated in Figure 3. In this figure, the ROE are

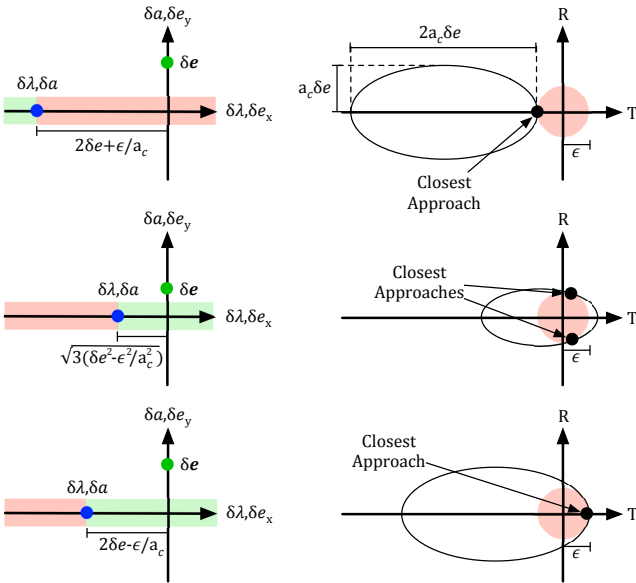


Fig. 3. Limit cases for safe separation in the RT-plane.

shown on the left and the corresponding relative motion in the RT-plane is shown on the right. The upper plot shows a formation in which the deputy does not encircle the chief and the middle and lower plots show formations in which the deputy encircles the chief. In each case, the formation will have a safe minimum separation if  $\delta \lambda$  is in the green region. It is noteworthy that the point of closest approach is not unique in the middle

plot. This is because the magnitude of the relative eccentricity vector is in the range  $\epsilon \leq a_c \delta e < 2\epsilon$ . As a result, the radius of curvature of the narrow end of the relative motion ellipse is less than  $\epsilon$ . For  $a_c \delta e \geq 2\epsilon$ , the radius of curvature is always greater than  $\epsilon$ , resulting in a unique point of closest approach at the limiting value of  $\delta \lambda$ .

Finally, it is necessary to consider the coupling between effects of differential drag and the collision avoidance constraints. Since differential drag causes a drift in  $\delta e$ , it is possible that this perturbation could cause the formation to violate the  $e/i$  vector separation constraint in Eq. (11). However, it is likely that  $\delta \lambda$  will be sufficiently large to ensure collision avoidance in the RT-plane long before this becomes an issue. On the other hand, the constraints in Eq. (14) place an upper bound on  $|\delta \lambda|$  that scales with  $\delta e$ . Because the largest effect of differential drag manifests in  $\delta \lambda$ , it is evident that formations relying on the constraint in Eq. (14) will require frequent maneuvers to counteract the effects of differential drag.

### 3. Swarm Formation Design

The models reviewed in the previous section for binary formations can now be generalized to spacecraft swarms. In this paper a swarm is modeled as a mothership with  $N$  deputies. However, the presented guidance and control techniques can also be applied to a swarm model where the mothership is replaced with a virtual reference that is known by all spacecraft in the swarm. In principle, it is possible to ensure collision-free relative motion for the entire swarm by verifying that at least one of the constraints in Eqs. (9), (13), or (14) is satisfied for every pair of spacecraft. However, the number of constraints that must be checked using this approach scales quadratically with the number of spacecraft,<sup>22</sup> incurring a significant computational cost when applied to large swarms. To mitigate this issue, a new method to verify collision avoidance between all spacecraft in a swarm including uncertainty is presented in the following. The key advantage of this method is that the computation cost scales linearly with the number of spacecraft. As a result, use of this method reduces the computational requirements of the GN&C system, potentially reducing the cost of each spacecraft or enabling more complex payloads. The method is applied to two swarm formations that ensure a passive minimum separation in the RT- and RN-planes, respectively, in the following.

#### 3.1. Math Model

In order to model spacecraft swarms, it is first necessary to establish a convention for describing the relative states between all of the spacecraft. In this paper the relative state of the  $j$ th deputy with respect to the mothership is denoted  $\delta \alpha_j$  and the relative state of the  $k$ th deputy with respect to the  $j$ th deputy is denoted  $\delta \alpha_{jk}$ . Under this convention, the relationship between the relative states of the deputies is given to first order by

$$\delta \alpha_{jk} = \delta \alpha_k - \delta \alpha_j \quad \delta \alpha_{jk} = -\delta \alpha_{kj} \quad (15)$$

It is noted that this model is exact when each spacecraft in the swarm has the same semimajor axis and inclination, as seen from the definition of the ROE in Eq. (1). This model can be used to simplify the swarm design problem as demonstrated in the following. First, recall from the previous section that the

relative motion of two spacecraft in  $J_2$ -perturbed near-circular orbits will be passively bounded if  $\delta a = 0$  and  $\delta i_x = 0$ . To achieve the same property for a swarm, it is necessary that all  $\delta a_j$ ,  $\delta a_{jk}$ ,  $\delta i_{x,j}$ , and  $\delta i_{x,jk}$  are zero. This condition is only satisfied if all spacecraft in the swarm have the same semimajor axis and inclination. In light of this result, it is hereafter assumed that the orbits of all spacecraft in the swarm have the same semimajor axis and inclination and the subscript  $c$  is dropped from these terms to simplify notation. Next, suppose that  $\delta \alpha$  satisfies one of the constraints in Eqs. (9) and (14). By inspecting these equations, it can be seen that the constraint will still be satisfied if  $\delta \alpha$  is multiplied by any constant with an absolute value of at least one. The combination of this property and the linear relationship between the relative states of the deputies suggests that passively safe swarm formations can be developed by simply distributing all  $\delta \alpha_j$  in ROE space in a regular pattern with some minimum spacing. In such a configuration, separation between the closest pair of spacecraft implies separation between all spacecraft in the swarm. This approach is used to derive swarm formations that satisfy Eqs. (11) and (14) in the following.

### 3.2. High-Density Formation Design

The swarm formation design presented in the following seeks to maximize the number of spacecraft that can be deployed in a specified volume. To accomplish this, it is first necessary to determine if the number of spacecraft that can safely be deployed in a specified region scales with the area or volume of the region. From Eq. (8), the cross-track relative position can be expressed as a linear function of  $\delta i$  given by

$$\delta r_N = a \sin(u_c) \delta i_x - a \cos(u_c) \delta i_y \quad (16)$$

Since  $\delta i_x$  is zero to avoid drift due to  $J_2$ , it can be seen that the cross-track separation will be zero at the extreme latitudes ( $u_c = 90^\circ$  or  $270^\circ$ ). It follows that the entire swarm will be coplanar at these locations. As a result, the number of spacecraft that can be deployed in a specified volume must scale with the area in the RT-plane spanned by the swarm to ensure a safe minimum separation. With this in mind, consider a swarm formation that is only separated in the RT-plane. One way to distribute such a swarm is to space the deputies evenly along a set of non-intersecting relative orbits as proposed by Morgan.<sup>22)</sup> From Eq. (8) it is clear that the ellipses traced by two deputies about the mothership will only be concentric if  $\delta a$  and  $\delta \lambda$  are both zero. It follows that such a swarm is constructed by simply distributing the ROE of the deputies in relative eccentricity vector space. Additionally, if  $\delta \lambda$  is zero, the minimum separation between a pair of spacecraft separated only in relative eccentricity vector space is  $a \delta e$ . It follows that a sufficient condition to ensure a minimum separation of  $\epsilon$  between all spacecraft in a swarm such that all  $\delta \lambda_{jk}$  are zero is that all  $\delta e_j$  are distributed in a manner that satisfies

$$a \|\delta e_j - \delta e_k\|_2 \geq \epsilon \quad \forall j \neq k \quad (17)$$

The density of such a formation is maximized by distributing the relative eccentricity vectors in a grid of equilateral triangles as illustrated in Figure 4. In this figure, the red circles denote regions where the minimum separation with respect to at least one of the spacecraft is less than  $a \delta e_{sep}$ . It follows that additional spacecraft can only be added in the white region without

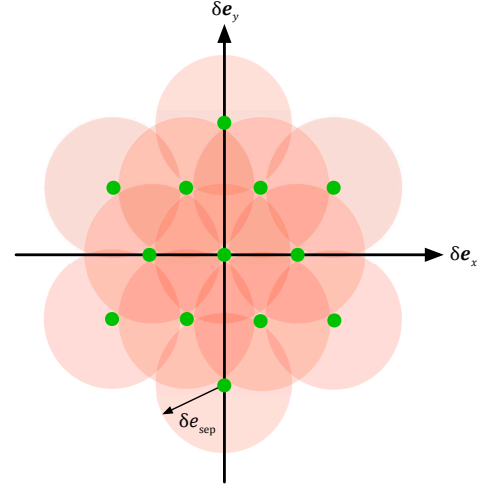


Fig. 4. Maximum density  $\delta e$  distribution.

decreasing the minimum separation between any pair of spacecraft. Additionally,  $a \delta e_{sep}$  must be at least  $\epsilon$  to satisfy Eq. (17). This formation can be constructed by expressing each  $\delta e_j$  as

$$\delta e_j = \begin{pmatrix} \delta e_{sep}(W_j \cos(\theta) + X_j \cos(\theta + 60^\circ)) \\ \delta e_{sep}(W_j \sin(\theta) + X_j \sin(\theta + 60^\circ)) \end{pmatrix} \quad (18)$$

where  $W_j$  and  $X_j$  are integers and  $\theta$  is the same for all spacecraft in the swarm. It is required that  $W_j$  and  $X_j$  cannot both be zero to avoid colliding with the mothership. Additionally, they cannot simultaneously satisfy  $W_j = W_k$  and  $X_j = X_k$  for any  $j \neq k$  to provide a unique relative eccentricity vector for each deputy. The  $60^\circ$  degree separation between the basis vectors in this formula ensures that the deputies are arranged in the aforementioned grid of equilateral triangles.

In order to allow such a formation to be used in a real mission, it is necessary to account for uncertainty. With this in mind, suppose that the relative eccentricity vector of each deputy is known to be within some  $3\text{-}\sigma$  uncertainty margin  $\sigma_{\delta e}$  of its nominal value defined from Eq. (18). Next, consider the worst-case separation between two adjacent deputies in  $\delta e$  space. The minimum separation occurs when each deputy is displaced by  $\sigma_{\delta e}$  towards the adjacent deputy. Thus, the minimum separation  $\delta e_{min}$  between any two  $\delta e_j$  is given by

$$\delta e_{min} = \delta e_{sep} - 2\sigma_{\delta e} \quad (19)$$

Following from Eq. (14), a sufficient condition to ensure that all spacecraft have a minimum separation of  $\epsilon$  in the RT-plane is given by

$$a |\delta \lambda_{jk}| \leq f(a, \delta e_{min}, \epsilon) \quad \forall j \neq k \quad (20)$$

where  $f$  is defined in Eq. (14). Next, suppose that each  $\delta \lambda_j$  satisfies

$$a |\delta \lambda_j| \leq \frac{f(a, \delta e_{min}, \epsilon)}{2} \quad (21)$$

It follows that all  $\delta \lambda_{jk}$  must satisfy

$$a |\delta \lambda_{jk}| = a |\delta \lambda_k - \delta \lambda_j| \leq a |\delta \lambda_k| + a |\delta \lambda_j| \leq f(a, \delta e_{min}, \epsilon) \quad (22)$$

Thus, constraining each  $\delta \lambda_j$  to satisfy Eq. (21) is sufficient to ensure a minimum separation of  $\epsilon$  in the RT-plane between all spacecraft in a swarm with the nominal distribution defined in Eq. (18) with uncertainty as large as  $\sigma_{\delta e}$ . This constraint only

needs to be checked for the relative state of each deputy with respect to the mothership, so the computational cost of ensuring collision avoidance scales linearly with the number of spacecraft. Furthermore, this constraint is less strict than the condition proposed by Morgan<sup>22</sup> that all relative orbits should be non-intersecting. An example formation that satisfies Eq. (21) with intersecting relative orbits is shown in Figure 5. This for-

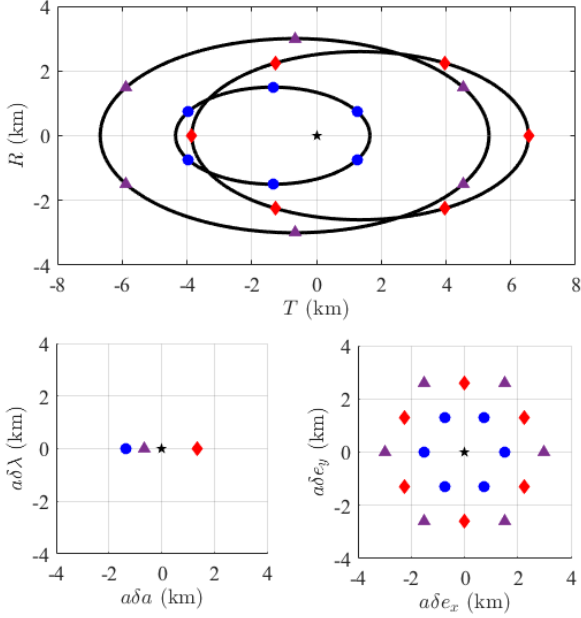


Fig. 5. Example of passively safe intersecting relative orbits in RT-plane (top) and ROE space (bottom).

mation is configured such that  $a\delta e_{sep}$  is 1.5 km and all  $a|\delta\lambda_j|$  are no larger than 1.35 km, which is sufficient to guarantee a minimum separation of 100 m with an uncertainty of 50 m in the relative eccentricity vector of each deputy. This figure shows three relative orbits with six deputies each. The centers of the relative orbits are specified by  $\delta\lambda$  (bottom left plot). It can be seen that the spacecraft in the smallest and largest relative orbits (blue circles and purple triangles) have the same phasing, as expected since the phase angles of the relative eccentricity vectors are the same. However, the phasing of the spacecraft on the middle relative orbit (red diamonds) is offset, ensuring a safe separation at the intersection of the relative orbits. The reason for this behavior is that separation in relative eccentricity vector space accounts for the difference in both magnitude and phasing of the relative orbits, allowing passive safety to be ensured with larger along-track separations.

### 3.3. Formation Design Using E/I Vector Separation

A significant limitation of the high-density formation design is that frequent maneuvers will be required to counteract the effect of differential drag on  $\delta\lambda$ . Considering the limited on-board resources of small satellites, a formation design that allows the swarm to passively drift for an extended time period could improve mission performance. Specifically, the spacecraft would be free to collect measurements, recharge batteries, align the antenna to communicate with a ground station, or perform any other operations required by the mission during these passive drift phases. As described in Sec. 2, the relative eccentricity/inclination vector concept developed by D'Amico ensures a

passive minimum separation in the RN-plane provided that the dot product of  $\delta e$  and  $\delta i$  is sufficiently large. As a result, the drift of  $\delta\lambda$  due to differential drag does not pose a collision risk. Following from Eq. (10), the necessary condition to ensure a minimum RN-plane separation of  $\epsilon$  between all spacecraft in a swarm is given as

$$|\delta e_{jk} \cdot \delta i_{jk}| \geq \frac{\epsilon}{a} \sqrt{\delta e_{jk}^2 + \delta i_{jk}^2} - \frac{\epsilon}{a} \quad \forall j \neq k \quad (23)$$

Once again the cost of verifying this constraint scales quadratically with the number of spacecraft. However, it is possible to use the technique employed in the high-density formation design to ensure collision avoidance between all pairs of spacecraft at reduced computational cost. Suppose that the relative eccentricity and inclination vectors of the  $j$ th deputy are defined as

$$\delta e_j = Y_j \delta e_{sep} \begin{pmatrix} \cos(\theta) \\ \sin(\theta) \end{pmatrix} \quad \delta i_j = Z_j \delta i_{sep} \begin{pmatrix} 0 \\ 1 \end{pmatrix} \quad (24)$$

where  $\delta e_{sep}$ , and  $\delta i_{sep}$ , and  $\theta$  are constants for the swarm and  $Y_j$  and  $Z_j$  are nonzero integers that satisfy

$$Y_j \neq Y_k, \quad Z_j \neq Z_k \quad \forall j \neq k \quad (25)$$

This constraint ensures that the relative eccentricity and inclination vectors for the deputies are unique. An example swarm in this configuration is shown in Figure 6. Using the relation-

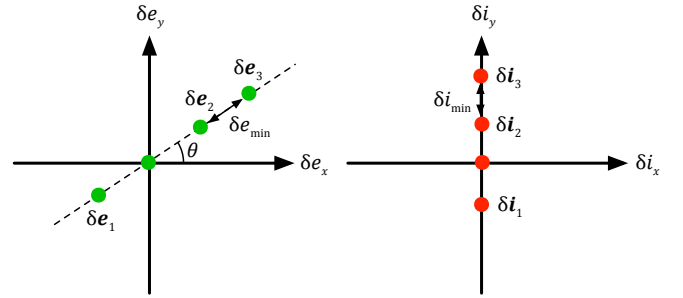


Fig. 6. Example swarm formation using e/i vector separation.

ship between the states of the deputies in Eq. (15), the relative eccentricity and inclination vectors between any two deputy spacecraft can be expressed as

$$\delta e_{jk} = Y_{jk} \delta e_{sep} \begin{pmatrix} \cos(\theta) \\ \sin(\theta) \end{pmatrix} \quad \delta i_{jk} = Z_{jk} \delta i_{sep} \begin{pmatrix} 0 \\ 1 \end{pmatrix} \quad (26)$$

where  $Y_{jk} = Y_k - Y_j$  and  $Z_{jk} = Z_k - Z_j$ . Substituting these expressions into Eq. (10) yields

$$|Y_{jk} Z_{jk} \delta e_{sep} \delta i_{sep} \sin(\theta)| \geq \frac{\epsilon}{a} \sqrt{Y_{jk}^2 \delta e_{sep}^2 + Z_{jk}^2 \delta i_{sep}^2} - \frac{\epsilon}{a} \quad (27)$$

Since  $Y_{jk}$  and  $Z_{jk}$  must be nonzero integers, the limiting case of Eq. (27) is given as

$$|\sin(\theta)| \geq \frac{\epsilon}{a \delta e_{sep} \delta i_{sep}} \sqrt{\delta e_{sep}^2 + \delta i_{sep}^2} - \frac{\epsilon}{a} \quad (28)$$

It can be seen that any formation satisfying Eq. (28) will also satisfy Eq. (27) for any nonzero  $Y_{jk}$  and  $Z_{jk}$ . It follows that if the closest pair of spacecraft in a swarm configured according to Eq. (24) has a minimum separation of  $\epsilon$  in the RN-plane, then

all pairs of spacecraft in the swarm will also have a minimum separation of at least  $\epsilon$ .

Next, these constraints can be modified to include uncertainty. Suppose that all  $\delta e_j$  and  $\delta i_j$  are known to be within  $3\text{-}\sigma$  uncertainty margins  $\sigma_{\delta e}$  and  $\sigma_{\delta i}$ , respectively, of their nominal values as defined in Eq. (24). The smallest possible magnitude of any  $\delta e_{jk}$  is given in Eq. (19) and the smallest magnitude of any  $\delta i_{jk}$ , denoted  $\delta i_{min}$ , is given by

$$\delta i_{min} = \delta i_{sep} - 2\sigma_{\delta i} \quad (29)$$

Additionally, because the minimum RN-plane separation depends on the dot product between the relative eccentricity and inclination vectors, it is possible that rotations of  $\delta e_{jk}$  and  $\delta i_{jk}$  can violate the constraint in Eq. (27). The worst-case rotation of the relative eccentricity vector between two adjacent deputies  $\delta\theta$  due to an uncertainty of  $\sigma_{\delta e}$  is illustrated in Figure 7. As

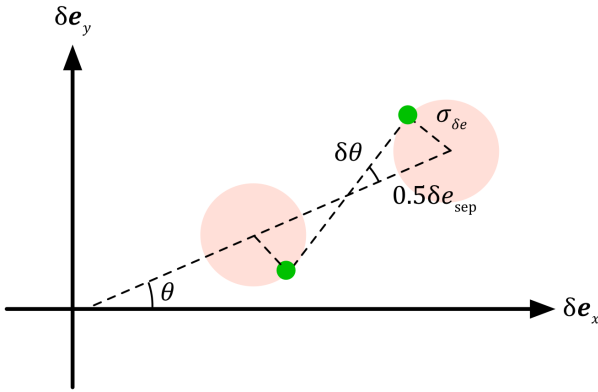


Fig. 7. Worst-case arrangement of adjacent deputies within  $\sigma_{\delta e}$  uncertainty margins that maximizes rotation  $\delta\theta$  of  $\delta e_{jk}$ .

shown in the figure, the worst-case rotation is obtained when the line connecting the two deputies is tangent to the boundaries of both uncertainty regions (red circles). From simple trigonometry,  $\delta\theta$  and the worst-case rotation of the relative inclination vector  $\delta\varphi$  are given by

$$\delta\theta = \arcsin\left(\frac{2\sigma_{\delta e}}{\delta e_{sep}}\right) \quad \delta\varphi = \arcsin\left(\frac{2\sigma_{\delta i}}{\delta i_{sep}}\right) \quad (30)$$

Combining Eqs. (19) and (28-30), a sufficient constraint to ensure a minimum RN-plane separation of  $\epsilon$  between all spacecraft in the presence of uncertainty in  $\delta e$  and  $\delta i$  is given by

$$|\sin(\theta + \psi)| \geq \frac{\epsilon}{a\delta e_{min}\delta i_{min}} \sqrt{\delta e_{min}^2 + \delta i_{min}^2} - \frac{\epsilon}{a} \quad (31)$$

$$\psi = -\text{sign}(\tan(\theta))(\delta\theta + \delta\varphi)$$

where  $\psi$  is the sum of the worst-case rotations of the relative eccentricity and inclination vectors between two deputies. This equation can be used to determine what separation is needed to ensure safe RN-plane separation at a specified  $\theta$  for a given uncertainty. Also, because  $\theta$  will rotate due to  $J_2$  unless maneuvers are performed, this constraint can also be used to determine how long the formation can be allowed to drift before maneuvers are required to ensure safe separation in the RT-plane. It should be noted that Eq. (31) is a sufficient, but not necessary constraint because the worst-case separations and rotations of the relative eccentricity and inclination vectors do not occur simultaneously.

## 4. Control Design

As demonstrated in Sec. 2, differential drag causes drifts in the in-plane ROE that must be corrected periodically to ensure safe and bounded relative motion for both of the described formation designs. The control architecture presented in the following is derived under the assumption that the guidance profile follows the passive rotation of the relative eccentricity vector due to  $J_2$  described in Eq. (3). Thus, control input is only needed to counteract the effects of differential drag. To meet this need, a nonlinear bang-off-bang state space control law is derived that ensures that  $\delta a$  and  $\delta\lambda$  remain near zero and that  $\delta e$  remains close to the desired reference with minimal actuation. For the formation design using e/i vector separation, this control law is implemented in a hybrid passive/active architecture that periodically allows the spacecraft to freely drift and only commands maneuvers when necessary. Specifically, this architecture commands maneuvers 1) when the phase angle of the relative eccentricity vectors will soon violate the constraint defined in Eq. (31), resulting in insufficient RN-plane separation, and 2) at regular intervals to ensure that the inter-spacecraft separation stays within user-specified limits. For the high-density swarm design, the control law is engaged at all times. Before deriving the control law, it is necessary to establish a model of the relationship between performed maneuvers and their effects on the ROE. In near-circular orbits, the time derivatives of the ROE corresponding to a relative acceleration  $\delta p$  in the RTN frame applied to the deputy are given by D'Amico<sup>5)</sup> as

$$\delta\dot{\alpha}(t) = \mathbf{\Gamma}(\alpha_c(t))\delta p(t) = \mathbf{\Gamma}(\alpha_c(t)) \begin{pmatrix} \delta p_R(t) \\ \delta p_T(t) \\ \delta p_N(t) \end{pmatrix}$$

$$\mathbf{\Gamma}(\alpha_c(t)) = \frac{1}{an} \begin{bmatrix} 0 & 2 & 0 \\ -2 & 0 & 0 \\ \sin(u_c) & 2\cos(u_c) & 0 \\ -\cos(u_c) & 2\sin(u_c) & 0 \\ 0 & 0 & \cos(u_c) \\ 0 & 0 & \sin(u_c) \end{bmatrix} \quad (32)$$

where  $\mathbf{\Gamma}$  is the control matrix. Using this model, the state at time  $t_0 + \tau$  is related to a prior state at time  $t_0$  and the control input profile by

$$\delta\alpha(t_0 + \tau) = \mathbf{\Phi}(\alpha_c(t_0), \tau)\delta\alpha(t_0) + \int_0^\tau \mathbf{\Phi}(\alpha_c(t_0 + t), \tau - t)\mathbf{\Gamma}(\alpha_c(t_0 + t))\delta p(t_0 + t)dt \quad (33)$$

The properties of this model can be used to simplify the control design problem. Specifically, it is evident from Eq. (32) that the most efficient way to change  $\delta a$  and  $\delta e$  is by performing a maneuver in the along-track direction. Additionally, a change in  $\delta\lambda$  can be efficiently generated by performing a pair of equal and opposite along-track maneuvers separated by a reasonable time ( $\geq 0.25$  orbits). It follows that all of the in-plane ROE can be efficiently controlled using only along-track maneuvers. With this in mind, two nonlinear bang-off-bang state space control laws are formulated using low-thrust and differential drag control in order to provide safe and bounded relative motion for both of the swarm designs presented in Sec. 3. Differential drag control be implemented by changing the attitude of the deputies to vary the cross-sectional area as routinely performed by the Dove telescope spacecraft in the Planet constellation.<sup>35)</sup>

#### 4.1. Low-Thrust Control

The nonlinear bang-off-bang low-thrust control law described in the following is inspired by recent work on impulsive control of spacecraft formations.<sup>28,29)</sup> The control command is computed in two steps. First, a preliminary commanded acceleration  $U_{\delta a, \delta \lambda}^{com}$  is computed as a function of  $\delta a$ ,  $\delta \lambda$ , a specified reconfiguration time, and the actuation capabilities of the spacecraft. The final commanded acceleration  $U^{com}$  is computed by modulating  $U_{\delta a, \delta \lambda}^{com}$  to ensure that performed maneuvers have a favorable effect on  $\delta e$ .

##### 4.1.1. Control Law for $\delta a$ and $\delta \lambda$

The primary goal of the control law for  $\delta a$  and  $\delta \lambda$  is to counteract the along-track drift caused by differential drag. However, before deriving the state space control law, it is insightful to first show the behavior of ROE control using a simple example. Consider the problem of changing  $\delta \lambda$  from some nonzero initial value  $\delta \lambda(t_0)$  to zero in a specified time  $\Delta t_{rec}$  using low-thrust control. In this example it is assumed that the initial and final values of  $\delta a$  are zero. Neglecting the effect of maneuvers on the relative eccentricity vector, the minimum delta-v maneuver sequence for these reconfiguration includes two equal and opposite maneuvers at the beginning and end, respectively, of the propagation.<sup>28,29)</sup> The first maneuver increases  $|\delta a|$  such that  $\delta \lambda$  drifts toward zero. At the end of the propagation, the second maneuver drives  $\delta a$  back to zero. This maneuver sequence is illustrated in Figure 8. Considering only maneuvers in the

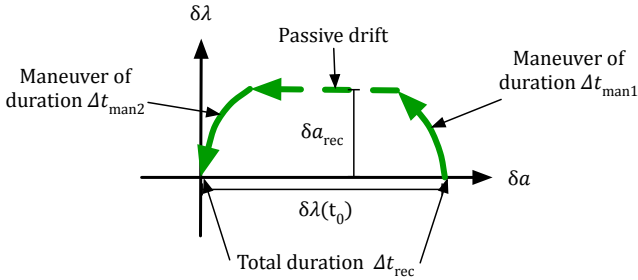


Fig. 8. Reconfiguration maneuver sequence to drive  $\delta \lambda$  to zero in time  $\Delta t_{rec}$ .

along-track direction for spacecraft in unperturbed near-circular orbits, the STM and control input matrices for this problem are given by D'Amico<sup>5)</sup> as

$$\Phi(\alpha_c(t), \tau) = \begin{bmatrix} 1 & 0 \\ -1.5n\tau & 1 \end{bmatrix} \quad \Gamma(\alpha_c(t)) = \begin{bmatrix} 2/(an) \\ 0 \end{bmatrix} \quad (34)$$

Let  $U$  denote the acceleration produced by the thrusters,  $\Delta t_{man1}$  and  $\Delta t_{man2}$  denote the duration of each of the maneuvers, and  $\Delta t_{rec}$  denote the total reconfiguration time. In order to reconfigure the formation as described, these values must satisfy Eq. (33) for the given initial and final conditions. From Eqs. (33) and (34), the governing equation for  $\delta a$  is given by

$$\delta a(t_0 + \Delta t_{rec}) = \delta a(t_0) + \frac{2U}{an} \Delta t_{man1} - \frac{2U}{an} \Delta t_{man2} \quad (35)$$

Since the initial and final values of  $\delta a$  are zero from the problem definition, it is evident that this equation is only satisfied if  $\Delta t_{man1} = \Delta t_{man2}$ . To simplify notation in the following derivations, the numeric subscripts for these maneuver durations are

dropped. From Eqs. (33) and (34), the governing equation for  $\delta \lambda$  for this problem is given by

$$\delta \lambda(t_0) - \frac{3U}{a} \Delta t_{man} (\Delta t_{rec} - \Delta t_{man}) = 0 \quad (36)$$

Using this equation, it is possible to solve for the duration of each maneuver in closed-form for a specified thrust value and initial condition. This maneuver duration is given by

$$\Delta t_{man} = \frac{\Delta t_{rec} - \sqrt{\Delta t_{rec}^2 - \frac{4a|\delta \lambda(t_0)|}{3U}}}{2} \quad (37)$$

This equation only has a real solution for  $\Delta t_{man} \leq \Delta t_{rec}/2$ . Accordingly,  $\Delta t_{rec}$  must satisfy

$$\Delta t_{rec} \geq \sqrt{\frac{4a|\delta \lambda(t_0)|}{3U}} \quad (38)$$

for a feasible maneuver sequence to exist. Finally, the total delta-v cost of the maneuver sequence  $\Delta v_{rec}$  is computed by multiplying the applied thrust by the total maneuver time. Using the single maneuver time from Eq. (37), this delta-v cost is given by

$$\Delta v_{rec} = U \left( \Delta t_{rec} - \sqrt{\Delta t_{rec}^2 - \frac{4a|\delta \lambda(t_0)|}{3U}} \right) \quad (39)$$

Next, the solution of this example problem is used to derive a nonlinear bang-off-bang state space control law that produces the described series of maneuvers for any  $\delta \lambda(t_0)$ . Without loss of generality, assume that  $\delta \lambda(t_0)$  is positive. During the second maneuver of the described sequence,  $\delta a$  and  $\delta \lambda$  can be written as explicit functions of time. If the second maneuver ends at time  $t$ , then these functions are given as

$$\delta a(t - \tau) = \frac{2U}{an} \tau \quad \delta \lambda(t - \tau) = \frac{3U}{2a} \tau^2 \quad (40)$$

By factoring out  $\tau$ , it is found that the second maneuver follows a path given by

$$\delta \lambda = \frac{3an^2}{8U} \delta a^2 \quad (41)$$

From Eq. (32), the duration of the maneuver that drives  $\delta a$  and  $\delta \lambda$  from a point on this line to the origin is given by

$$\Delta t_{man} = \frac{an}{2U} \delta a \quad (42)$$

Also, there will be a drift period between the maneuvers of duration  $\Delta t_{rec} - 2\Delta t_{man}$ . The location of the start of this drift can be computed by adding the change in  $\delta \lambda$  over this time from Eq. (33) to the location of the end of the drift (and start of the second maneuver) in Eq. (41). Combining these expressions, the line defining the end of the first maneuver is given by

$$\delta \lambda = \frac{3}{2} n \delta a \left( \Delta t_{rec} - \frac{3an}{4U} \delta a \right) \quad (43)$$

Equations (41) and (43) parametrically define the boundaries of the required maneuvers provided that  $\delta \lambda(t_0)$  is nonnegative. If  $\delta \lambda(t_0)$  is negative, these equations simply have opposite signs.

It is now possible to define a nonlinear bang-off-bang control law to produce the described maneuver sequence. Because the output of this control law will be modulated to ensure a favorable effect on  $\delta e$ , a modified acceleration parameter  $U^*$  is

adopted to ensure that the spacecraft can follow the switching lines of the control law. This parameter is the maximum acceleration that is guaranteed to be consistent with the modulated maneuvers and is defined in the following section. Using the results from Eqs. (41) and (43), the switching lines for thrust in the flight direction  $\Lambda_{thrust}^+$  and anti-flight direction  $\Lambda_{thrust}^-$  are given as a function of  $\delta a$  and constant parameters  $\Delta t_{rec}$  and  $U^*$  by

$$\Lambda_{thrust}^+(\delta a) = \begin{cases} \frac{3an^2}{8U^*}\delta a^2 + \delta\lambda_{wait} & \text{if } \delta a \geq 0 \\ -\frac{3an^2}{8U^*}\delta a^2 & \text{if } \delta a < 0 \end{cases} \quad (44)$$

$$\Lambda_{thrust}^-(\delta a) = \begin{cases} \frac{3an^2}{8U^*}\delta a^2 & \text{if } \delta a \geq 0 \\ -\frac{3an^2}{8U^*}\delta a^2 - \delta\lambda_{wait} & \text{if } \delta a < 0 \end{cases}$$

where  $\delta\lambda_{wait}$  is the change in  $\delta\lambda$  due to the drift between maneuvers, which is given by

$$\delta\lambda_{wait} = \frac{3}{2}|\delta a| \max\left(\Delta t_{rec} - \frac{an}{U^*}|\delta a|, 0\right) \quad (45)$$

The preliminary commanded acceleration  $U_{\delta a, \delta\lambda}^{com}$  is given by

$$U_{\delta a, \delta\lambda}^{com}(\delta a, \delta\lambda) = \begin{cases} U & \text{if } \delta\lambda \geq \Lambda_{thrust}^+(\delta a) \\ -U & \text{if } \delta\lambda \leq \Lambda_{thrust}^-(\delta a) \\ 0 & \text{otherwise} \end{cases} \quad (46)$$

The control regions are shown in Figure 9 for  $U^*$  of  $10^{-5}$  m/s<sup>2</sup> and  $\Delta t_{rec}$  of three orbits along with an example trajectory. In

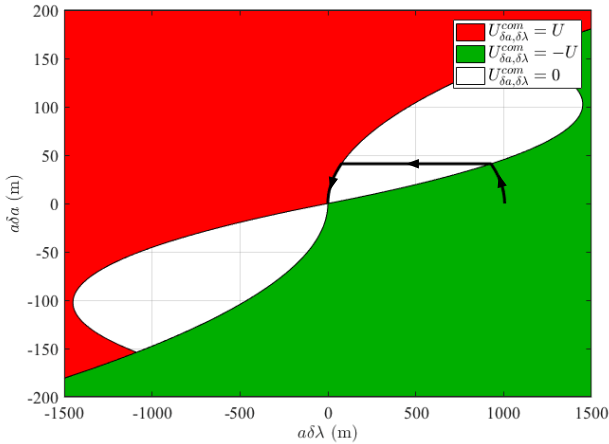


Fig. 9. Commanded acceleration  $U_{\delta a, \delta\lambda}^{com}$  defined from Eq. (46) using switching lines defined in Eq. (44) with example trajectory.

addition to exactly replicating the previously described reconfiguration sequence, this control law will drive  $\delta\lambda(t_0)$  to zero in minimum time if doing so in  $\Delta t_{rec}$  is infeasible.

However, it is noteworthy that the switching lines for both control regions go through the origin. This will cause rapid changes in the commanded acceleration when implemented on a system with realistic navigation errors, increasing propellant consumption. To mitigate this issue, a deadband can be introduced to the controller to smooth the commanded actuation profile in the presence of navigation errors. The switching

lines including a deadband of  $\delta\lambda_{db}$  for thrust in the flight direction  $\Lambda_{thrust,db}^+$  and anti-flight direction  $\Lambda_{thrust,db}^-$  are given by

$$\Lambda_{thrust,db}^+(\delta a) = \begin{cases} \max(-\delta\lambda_{db} + \frac{3an^2}{8U^*}\delta a^2 + \delta\lambda_{wait}, \delta\lambda_{db}) & \text{if } \delta a \geq 0 \\ \delta\lambda_{db} - \frac{3an^2}{8U^*}\delta a^2 & \text{if } \delta a < 0 \end{cases} \quad (47)$$

$$\Lambda_{thrust,db}^-(\delta a) = \begin{cases} -\delta\lambda_{db} + \frac{3an^2}{8U^*}\delta a^2 & \text{if } \delta a \geq 0 \\ \min(\delta\lambda_{db} - \frac{3an^2}{8U^*}\delta a^2 - \delta\lambda_{wait}, -\delta\lambda_{db}) & \text{if } \delta a < 0 \end{cases}$$

The control regions for the described deadband controller with  $a\delta\lambda_{db}$  of 50 meters are illustrated in Figure 10 including an example trajectory.

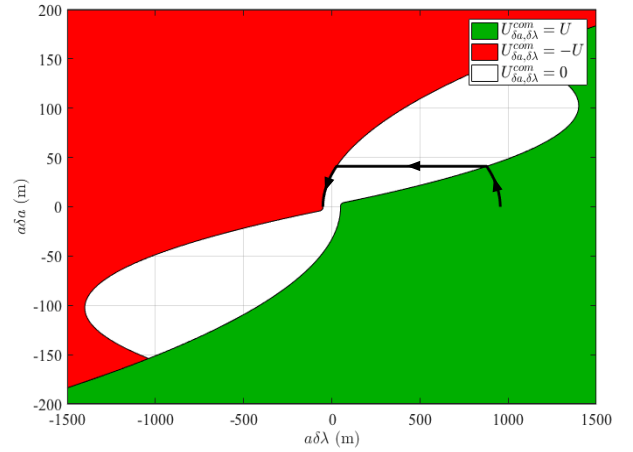


Fig. 10. Commanded acceleration  $U_{\delta a, \delta\lambda}^{com}$  defined from Eq. (46) using deadband switching lines defined in Eq. (47) with example trajectory.

#### 4.1.2. Control Law for $\delta e$

The objective of the relative eccentricity vector control law is to ensure that the relative eccentricity vectors of the deputies maintain a safe minimum spacing as defined in Eqs. (18) and (24). This is accomplished at minimum actuation cost by having the relative eccentricity of each deputy follow the passive rotation due to  $J_2$  defined in Eq. (3). An important consequence of the structure of the control matrix in Eq. (32) is that the change in  $\delta a$  caused by an along-track maneuver is equal to the path length traveled by the relative eccentricity vector. Additionally the phase angle of the change in the relative eccentricity vector depends on the location of the maneuver. This property suggests that the secular effect of differential drag on the relative eccentricity vector will be less than the change in  $\delta a$ . This property is exploited in the control design by simply modulating  $U_{\delta a, \delta\lambda}^{com}$  to ensure that performed maneuvers have a favorable effect on the relative eccentricity vector. Let the relative eccentricity error  $\delta e_{err}$  be defined as

$$\delta e_{err} = \delta e - \delta e_{des} \quad (48)$$

If the magnitude of  $\delta e_{err}$  is within the deadband  $\delta e_{db}$ , then the commanded acceleration is equal to  $U_{\delta a, \delta\lambda}^{com}$ . However, if  $\delta e_{err}$

is outside of the deadband, the commanded acceleration is zero unless the condition

$$-\text{sign}(U_{\delta a, \delta \lambda}^{com}) \frac{\delta \mathbf{e}_{err}}{\|\delta \mathbf{e}_{err}\|_2} \cdot \begin{pmatrix} \cos(u) \\ \sin(u) \end{pmatrix} \geq \cos(\zeta) \quad (49)$$

is satisfied where  $\zeta$  defines the maximum allowable angle between the desired change in the relative eccentricity vector and the change produced by a nonzero  $U_{\delta a, \delta \lambda}^{com}$ . If  $\zeta$  is less than  $\pi/2$ , this constraint requires that any performed maneuver must decrease the magnitude of  $\delta \mathbf{e}_{err}$ . Using this approach, the commanded acceleration  $U^{com}$  is given by

$$U^{com} = \begin{cases} U_{\delta a, \delta \lambda}^{com} & \text{if } \|\delta \mathbf{e}_{err}\|_2 \leq \delta e_{db} \\ U_{\delta a, \delta \lambda}^{com} & \text{if } -\frac{\text{sign}(U_{\delta a, \delta \lambda}^{com}) \delta \mathbf{e}_{err}}{\|\delta \mathbf{e}_{err}\|_2} \cdot \begin{pmatrix} \cos(u) \\ \sin(u) \end{pmatrix} \geq \cos(\zeta) \\ 0 & \text{otherwise} \end{cases} \quad (50)$$

This control law allows for a limit cycle in which the relative eccentricity vector traces a circle around the desired value of radius  $\delta e_{db}$ . Additionally, it is necessary to define the time-averaged thrust parameter  $U^*$  to ensure a feasible trajectory is defined in  $\delta a$  and  $\delta \lambda$ . This parameter is defined by considering the limiting cases of the modulation produced by the control law for the relative eccentricity vector. If  $\delta \mathbf{e}_{err}$  is outside of the deadband, then the control law allows maneuvers that span at least  $\zeta/\pi$  of the orbit. On the other hand, if  $\delta \mathbf{e}_{err}$  is inside the deadband, then the resulting maneuvers can trace out a path no longer than  $2\pi\delta e_{db}$  in an orbit. From Eq. (32), this corresponds to an average acceleration of  $an^2\delta e_{db}/2$ . From these two conditions, the maximum guaranteed time-averaged acceleration allowed by the relative eccentricity vector control law is given by

$$U^* = \min\left(\frac{\zeta}{\pi}U, \frac{1}{2}an^2\delta e_{db}\right) \quad (51)$$

Recall that  $\zeta$  should be no larger than  $\pi/2$  in order to drive  $\delta \mathbf{e}_{err}$  to within the deadband. It follows that  $\zeta/\pi \leq 0.5$ , which means that the deadband is the limiting factor for  $U^*$  if  $an^2\delta e_{db} \leq U$ . Thus, there is a tradeoff between control precision and control authority using this control approach. However, this constraint is not expected to impact control design if low-thrust control is used. For example, if  $U$  is on the order of  $10^{-5}$  m/s<sup>2</sup>, then  $a\delta e_{db}$  can be no larger than a few meters in LEO to satisfy this constraint.

#### 4.1.3. Hybrid Passive/Active Control Timing

In order to use this control law in a hybrid passive/active architecture, it is necessary to determine two additional parameters: 1) the maximum drift time  $\Delta t_{drift}$  for which the control law can be disengaged before the effects of differential drag cause  $|\delta a|$  or  $|\delta \lambda|$  to increase beyond specified limits  $\delta a_{max}$  and  $\delta \lambda_{max}$ , and 2) the reconfiguration time  $\Delta t_{rec}$  that is required to ensure that safe separation in the RT-plane is established before separation in the RN-plane decreases below safe levels. To determine these values, consider the following simplified scenario illustrated in Figure 11. In this scenario, a deputy spacecraft is allowed to freely drift from the origin under the effects of differential drag for time  $\Delta t_{drift}$  as shown by the red line. After the drift, two maneuvers are performed to drive  $\delta \lambda$  and  $\delta a$  back to zero in time  $\Delta t_{rec}$  as shown by the solid green lines. In this

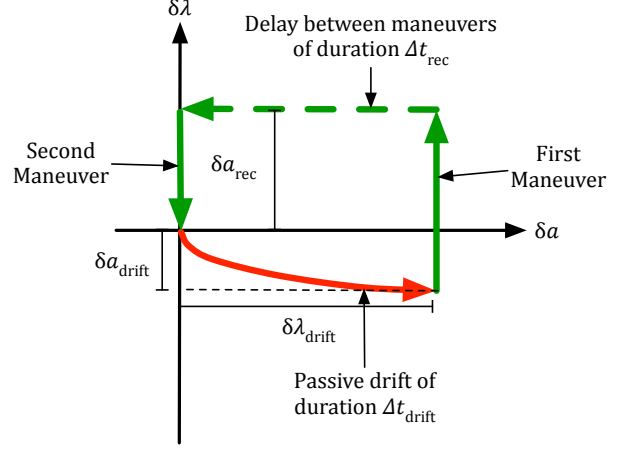


Fig. 11. Reconfiguration maneuver sequence for low-thrust control.

scenario it is assumed that  $\Delta t_{rec}$  is large relative to the maneuver duration, allowing the maneuvers to be reasonably approximated as impulsive. It is also assumed that  $\Delta t_{rec}$  is small in comparison to  $\Delta t_{drift}$ , so the effects of differential drag between the maneuvers can be neglected. Under the effects of differential drag, the relative semimajor axis drifts at a constant rate of  $\delta \dot{a}_{drag}$  and the evolution of  $\delta a$  and  $\delta \lambda$  can be modeled as

$$\begin{pmatrix} \delta a(t + \tau) \\ \delta \lambda(t + \tau) \end{pmatrix} = \begin{bmatrix} 1 & 0 \\ -\frac{3}{2}n & 1 \end{bmatrix} \begin{pmatrix} \delta a(t) \\ \delta \lambda(t) \end{pmatrix} + \delta \dot{a}_{drag} \begin{pmatrix} \tau \\ -\frac{3}{4}n\tau^2 \end{pmatrix} \quad (52)$$

If the drift starts at the origin, then the state after time  $\Delta t_{drift}$  is given by

$$\delta a_{drift} = \delta \dot{a}_{drag} \Delta t_{drift} \quad \delta \lambda_{drift} = -\frac{3}{4}n\delta \dot{a}_{drag} \Delta t_{drift}^2 \quad (53)$$

It is evident from this equation that  $\Delta t_{drift}$  must satisfy

$$\Delta t_{drift} \leq \min\left(\frac{\delta a_{max}}{|\delta \dot{a}_{drag}|}, \sqrt{\frac{4\delta \lambda_{max}}{3n|\delta \dot{a}_{drag}|}}\right) \quad (54)$$

to ensure that  $\delta a$  and  $\delta \lambda$  remain within the specified limits. After the drift phase, a maneuver is performed to change the relative semimajor axis to  $\delta a_{rec}$ , which ensures that  $\delta \lambda$  returns to zero after time  $\Delta t_{rec}$ . Since the final value of  $\delta \lambda$  must be zero and the effects of differential drag are neglected during the reconfiguration,  $\delta a_{rec}$  must satisfy

$$0 = \delta \lambda_{drift} - \frac{3}{2}n\delta a_{rec}\Delta t_{rec} \quad (55)$$

Substituting in the expressions from Eq. (53) and solving for  $\delta a_{rec}$  yields

$$\delta a_{rec} = -\frac{1}{2}\delta a_{drift} \frac{\Delta t_{drift}}{\Delta t_{rec}} \quad (56)$$

From this equation it is evident that  $\Delta t_{rec}$  must be selected to satisfy

$$\Delta t_{rec} \geq \frac{1}{2} \frac{|\delta \dot{a}_{drag}|}{\delta a_{max}} \Delta t_{drift}^2 = \frac{1}{2} \frac{|\delta a_{drift}|}{\delta a_{max}} \Delta t_{drift} \quad (57)$$

Because  $|\delta a_{drift}|/\delta a_{max}$  must be between zero and one, this constraint means that there is a lower bound on  $\Delta t_{rec}$  that approaches  $\Delta t_{drift}/2$  as  $|\delta a_{drift}|$  approaches  $\delta a_{max}$ . Next, suppose that the condition in Eq. (31) is known to be satisfied for some range  $\theta_{min} \leq \theta \leq \theta_{max}$ . In order to ensure that safe separation in

the RT-plane is achieved before RN-plane separation decreases below acceptable levels, it is necessary to select  $\Delta t_{drift}$  and  $\Delta t_{rec}$  such that

$$\Delta t_{drift} + \Delta t_{rec} \leq \frac{\theta_{max} - \theta_{min}}{\dot{\omega}_c} \quad (58)$$

Overall, selecting the drift and reconfiguration times to satisfy Eqs. (54), (57), and (58) is sufficient to simultaneously ensure collision avoidance and keep the entire reconfiguration profile within user-defined limits given an a-priori estimate of  $\delta \dot{a}_{drag}$ .

This model can also be used to estimate the total delta-v cost of the maneuvers in the reconfiguration sequence. It is clear from the trajectory shown in Figure 11 that the two maneuvers must produce a total change in  $\delta a$  of  $2|\delta a_{cont}| + |\delta a_{drift}|$ . The total delta-v cost of this reconfiguration  $\Delta v_{rec}$  can be found from Eq. (32) as

$$\begin{aligned} \Delta v_{rec} &= \frac{1}{2} an(2|\delta a_{rec}| + |\delta a_{drift}|) \\ &= \frac{1}{2} an|\delta a_{drift}| \left( \frac{\Delta t_{drift}}{\Delta t_{rec}} + 1 \right) \end{aligned} \quad (59)$$

It is evident from this equation that the cost associated with the pair of maneuvers depends on the duty cycle of the controller  $\Delta t_{rec}/\Delta t_{drift}$ . It follows that there is a trade space in the mission design between allowable drift time and control efficiency. For example, the duration of the drift phase can be maximized subject to the time constraint in Eq. (58) by minimizing the controller duty cycle. However, the resulting maneuver costs may be many times larger than those required to counteract  $\delta a_{drift}$ , resulting in inefficient control. Selecting a higher duty cycle requires shorter drift phases, but results in less propellant usage, which may extend the total mission lifetime. Additionally, this equation implies that the delta-v cost of the pair of maneuvers has a lower bound of  $an|\delta a_{drift}|/2$ , which is the cost of the maneuver required to negate the drift of  $\delta a$  due to differential drag.

#### 4.2. Differential Drag Control

Before deriving the differential drag control law, it is necessary to formalize a model of the effects of atmospheric drag. The perturbing acceleration due to atmospheric drag  $p_{drag}$  is directed in the anti-flight direction and has a magnitude given as

$$p_{drag} = \frac{1}{2} \rho v^2 \frac{C_D A}{m} \quad (60)$$

where  $\rho$  is the atmospheric density,  $v$  is the velocity of the spacecraft,  $C_D$  is the drag coefficient,  $A$  is the cross-section area, and  $m$  is the spacecraft mass. To simplify the following derivations, the ballistic properties of the spacecraft are captured in the ballistic coefficient  $B$ , which is defined as

$$B = \frac{C_D A}{m} \quad (61)$$

Additionally, for near-circular orbits, the velocity can be approximated as

$$v = na \quad (62)$$

Using these definitions, the acceleration due to atmospheric drag can be expressed as

$$p_{drag} = \frac{1}{2} \rho n^2 a^2 B \quad (63)$$

To model the effect of differential drag, let the differential ballistic coefficient  $\Delta B$  between a deputy and chief spacecraft be defined as

$$\Delta B = B_d - B_c \quad (64)$$

Provided that the spacecraft are in close proximity, the difference in directions between the velocity vectors can be neglected and the relative acceleration in the anti-flight direction due to differential drag  $\delta p_{drag}$  can be expressed as

$$\delta p_{drag} = \frac{1}{2} \rho a^2 n^2 \Delta B \quad (65)$$

From Eq. (32) the resulting drift of the relative semimajor axis due to differential drag is given as

$$\delta \dot{a}_{drag} = \rho an \Delta B \quad (66)$$

To simplify the control derivation, let  $\bar{\rho}$  denote the atmospheric density averaged over one orbit and let  $\Delta B_{max}$  be the largest achievable magnitude of  $\Delta B$  given the geometry of the spacecraft.

The differential drag control law uses the same architecture as the thrust control law, but includes small modifications to address the inherent limitations of this actuation strategy. First, the relative acceleration produced by differential drag maneuvers is generally within an order of magnitude of the perturbing acceleration, which means that the smallest achievable reconfiguration time will be comparable to or longer than the duration of the drift phase. Additionally, the changes in  $\delta a$  and  $\delta e$  produced by a differential drag maneuver are subject to high uncertainty deriving from two causes: 1) density variations over a single orbit due to the diurnal bulge, and 2) errors in atmospheric density models. Due to these limitations, a deputy using differential drag control may not be able to follow the switching line of the control law (illustrated in Figure 10), resulting in an overshoot of the deadband. In this case, multiple maneuver sequences will be required, resulting in a longer reconfiguration time. In light of these concerns,  $\delta \lambda_{wait}$  is set to zero in the differential drag control law to reduce the reconfiguration time. Additionally, because the atmospheric density varies over the orbit, the change in the relative eccentricity vector produced by a maneuver may not be in the desired direction. It is therefore possible that  $\delta a$  and  $\delta \lambda$  may reach their deadband before  $\delta e$ . This concern is addressed by adding a condition to the control law that produces a pair of equal and opposite maneuvers once per orbit if  $\delta a$  and  $\delta \lambda$  are within the deadband and  $\delta e$  is outside of the deadband. As before, it is also necessary to use a parameter  $\Delta B^*$  in the definition of the switching lines that defines the maximum time-averaged differential ballistic coefficient that is consistent with the modulation produced by the relative eccentricity vector control law. The switching lines for positive  $\Lambda_{drag}^+$  and negative  $\Lambda_{drag}^-$  differential ballistic coefficients are given by

$$\begin{aligned} \Lambda_{drag}^+(\delta a) &= \\ &\begin{cases} -\delta \lambda_{db} + \frac{3}{4\bar{\rho}a\Delta B^*} \delta a^2 & \text{if } \delta a \geq 0 \\ \min(\delta \lambda_{db} - \frac{3}{4\bar{\rho}a\Delta B^*} \delta a^2, -\delta \lambda_{db}) & \text{if } \delta a < 0 \end{cases} \\ \Lambda_{drag}^-(\delta a) &= \\ &\begin{cases} \max(-\delta \lambda_{db} + \frac{3}{4\bar{\rho}a\Delta B^*} \delta a^2, \delta \lambda_{db}) & \text{if } \delta a \geq 0 \\ \delta \lambda_{db} - \frac{3}{4\bar{\rho}a\Delta B^*} \delta a^2 & \text{if } \delta a < 0 \end{cases} \end{aligned} \quad (67)$$

and the preliminary control command  $\Delta B_{\delta a, \delta \lambda}^{com}$  is given by

$$\Delta B_{\delta a, \delta \lambda}^{com}(\delta a, \delta \lambda) = \begin{cases} \Delta B_{max} & \text{if } \delta \lambda \leq \Lambda_{drag}^+(\delta a) \\ -\Delta B_{max} & \text{if } \delta \lambda \geq \Lambda_{drag}^-(\delta a) \\ 0 & \text{otherwise} \end{cases} \quad (68)$$

The commanded actuation is plotted in the ROE state space for this control law in Figure 12 for an assumed  $\bar{\rho}$  of 1 g/km<sup>3</sup> (average for an orbit altitude of 450 km) and  $\Delta B^*$  of 0.005 m<sup>2</sup>/kg. In comparison with the control regions in Figures 9 and 10, it is evident that the maximum value of  $\delta a$  achieved in a reconfiguration of several hundred meters in  $a\delta\lambda$  will be less than 10 m, resulting in a reconfiguration time of at least several orbits.

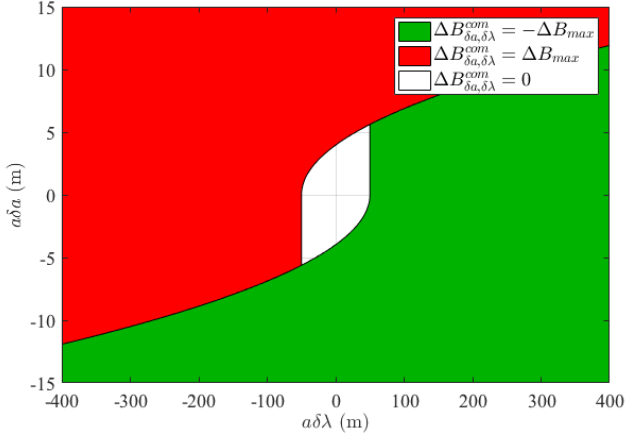


Fig. 12. Control regions for  $\Delta B_{\delta a, \delta \lambda}^{com}$  using switching lines defined in Eq. (67).

The final control command  $\Delta B^{com}$  is defined as

- If  $\|\delta e_{err}\|_2 \leq \delta e_{db}$ 
  - $\Delta B^{com} = \Delta B_{\delta a, \delta \lambda}^{com}$
- Else
  - If  $\Delta B_{\delta a, \delta \lambda}^{com} \neq 0$ 
    - If  $\text{sign}(\Delta B_{\delta a, \delta \lambda}^{com}) \frac{\delta e_{err}}{\|\delta e_{err}\|_2} \cdot \begin{pmatrix} \cos(u) \\ \sin(u) \end{pmatrix} \geq \cos(\zeta)$ 
      - $\Delta B^{com} = \Delta B_{\delta a, \delta \lambda}^{com}$
    - Else
      - $\Delta B^{com} = 0$
  - Else
    - If  $\frac{\delta e_{err}}{\|\delta e_{err}\|_2} \cdot \begin{pmatrix} \cos(u) \\ \sin(u) \end{pmatrix} \geq \cos(\zeta)$ 
      - $\Delta B^{com} = \Delta B_{max}$
    - Else if  $\frac{\delta e_{err}}{\|\delta e_{err}\|_2} \cdot \begin{pmatrix} \cos(u) \\ \sin(u) \end{pmatrix} \leq -\cos(\zeta)$ 
      - $\Delta B^{com} = -\Delta B_{max}$
    - Else
      - $\Delta B^{com} = 0$

The maximum achievable time-averaged differential ballistic coefficient is computed in the same way as  $U^*$  for the low-thrust control law. First, if  $\delta e_{err}$  is outside of the deadband, then a maneuvers are allowed that span at least  $\zeta/\pi$  of the orbit. If  $\delta e_{err}$  is inside the deadband, then the maneuver can cause a change in  $\delta a$  of no more than  $2\pi\delta e_{db}$  in a single orbit. Using Eq. (66), this corresponds to an average differential ballistic coefficient of  $\delta e_{db}/(\bar{\rho}a)$ . Thus,  $\Delta B^*$  is given by

$$\Delta B^* = \min\left(\frac{\zeta}{\pi}\Delta B_{max}, \frac{\delta e_{db}}{\bar{\rho}a}\right) \quad (69)$$

However, the relative acceleration produced by a differential drag maneuver is expected to be multiple orders of magnitude less than that of a maneuver performed with any thruster. As a result, only an extremely small deadband ( $a\delta e_{db}$  on the order of cm or smaller) will result in limited control authority.

Additionally, in order to use the hybrid passive/active control architecture with the swarm designs based on  $e/i$  vector separation, it is necessary to constrain the  $\Delta t_{drift}$  to ensure that safe separation in the RT-plane is established before RN-plane separation decreases below the minimum safe value and that  $\delta a$  and  $\delta \lambda$  stay within acceptable limits at all times. To simplify notation, the reconfiguration parameters are denoted by subscript  $rec$  as used in the timing analysis for low-thrust control. However, it should be noted that the formulas that govern these variables are different between low-thrust and differential drag control. To derive the necessary constraints, consider the following simplified model. As before, the spacecraft is allowed to freely drift for time  $\Delta t_{drift}$  under the effects of differential drag. At the end of the drift phase, the control law is engaged and the spacecraft performs two maneuvers to drive  $\delta a$  and  $\delta \lambda$  back to zero. This reconfiguration sequence is illustrated in Figure 13. Because the control is continuously engaged from the end of

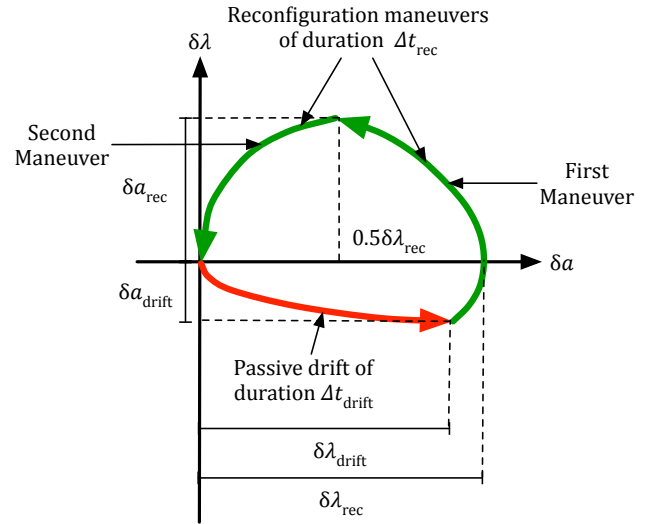


Fig. 13. Reconfiguration parameters for differential drag control.

the drift until  $\delta a$  and  $\delta \lambda$  are back in the deadband, the reconfiguration profile is fully specified by  $\Delta t_{drift}$  and a parameter  $D$  defined as

$$D = \frac{\delta \dot{a}_{rec}}{\delta \ddot{a}_{drag}} \quad (70)$$

where  $\delta \dot{a}_{rec}$  is the drift rate of  $\delta a$  achieved by a differential drag maneuver. In essence,  $D$  is a measure of the control authority using differential drag. This parameter can be approximated as the ratio of  $\Delta B^*$  to the residual differential ballistic coefficient when the commanded actuation is zero. The states at the end of the drift are the same as those specified in Eq. (53). However, because  $D$  cannot be assumed to be large, the continued drift after the start of the first maneuver cannot be neglected. Using the dynamics model in Eq. (52), the largest value of  $\delta \lambda$  reached during the reconfiguration  $\delta \lambda_{rec}$  is given as

$$\delta \lambda_{rec} = \delta \lambda_{drift} \left(1 + \frac{1}{D}\right) \quad (71)$$

After this condition is reached, the remaining maneuvers are equal and opposite. From this symmetry,  $\delta a_{rec}$  can be expressed as

$$\delta a_{rec} = \delta a_{drift} \sqrt{\frac{D+1}{2}} \quad (72)$$

and the total time required to perform both maneuvers  $\Delta t_{rec}$  is given by

$$\Delta t_{rec} = \Delta t_{drift} \frac{1 + \sqrt{2(D+1)}}{D} \quad (73)$$

From Eqs. (53) and (71), the necessary constraint to ensure that  $\delta \lambda_{rec}$  does not exceed  $\delta \lambda_{max}$  is given by

$$\Delta t_{drift} \leq \sqrt{\frac{4\delta \lambda_{max} D}{3n|\delta \dot{a}_{drag}|(D+1)}} \quad (74)$$

Similarly, the necessary constraint to ensure that  $\delta a_{rec}$  does not exceed  $\delta a_{max}$  can be derived from Eqs. (53) and (72). This constraint is given by

$$\Delta t_{drift} \leq \frac{\delta a_{max}}{|\delta \dot{a}_{drag}|} \sqrt{\frac{2}{D+1}} \quad (75)$$

Finally, it is necessary to ensure that Eq. (58) is satisfied in order to establish a safe minimum separation in the RT-plane before separation in the RN-plane decreases below acceptable levels. Substituting the expression for  $\Delta t_{rec}$  in Eq. (73) yields

$$\Delta t_{drift} \leq \frac{D}{D+1 + \sqrt{2(D+1)}} \frac{\theta_{max} - \theta_{min}}{\dot{\omega}_c} \quad (76)$$

The constraints in Eqs. (74), (75), and (76) are sufficient to ensure that the reconfiguration profile satisfies user-defined constraints and that safe separation in the RT-plane is established before RN-plane separation decreases below the acceptable limit. In order to minimize the control requirements placed on spacecraft in the swarm, it is desirable to minimize the ratio  $\Delta t_{rec}/\Delta t_{drift}$  to ensure long periods of free drift. From Eq. (73), it is clear that the duty cycle is minimized if  $D$  is as large as possible. Indeed, the ratio  $\Delta t_{rec}/\Delta t_{drift}$  can only be less than one if  $D$  is at least 4.25. However, it is simultaneously necessary to ensure that  $\delta a_{rec}$  does not exceed acceptable limits. With this in mind, it can be seen from Eq. (75) that  $\delta a_{rec}$  will be within a factor of three of  $\delta a_{drift}$  for  $D$  as large as 10. Since achieving such a large control authority using differential drag control requires a spacecraft with highly variable cross-sectional area, the constraint in Eq. (75) is not expected to drive selection of  $\Delta t_{drift}$  if the RN-plane separation is large relative to  $\delta a_{drift}$ .

## 5. Validation Scenario Definition

The swarm formations derived in Sec. 3 and control architectures derived in Sec. 4 are validated through simulation of a reference mission scenario. In this simulation, the swarm is modeled as a microsatellite mothership and a set of 18 nanosatellite deputies. The mothership is assumed to have a mass of 100 kg, a cross-section area of 1 m<sup>2</sup> and a drag coefficient of 1, resulting in a ballistic coefficient of 0.01 m<sup>2</sup>/kg. The deputy spacecraft are modeled after the 3U CubeSat telescope spacecraft used by Planet,<sup>35)</sup> which is shown in Figure 14. The modeled spacecraft have a mass of 4.5 kg, a drag coefficient of 0.9, and include a

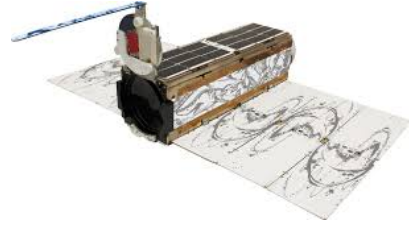


Fig. 14. CubeSat telescope spacecraft used by Planet.<sup>35)</sup>

0.3x0.7 m solar panel array. The sensing and actuation capabilities of the modeled spacecraft are based on the commercial-off-the-shelf (COTS) sensors and actuators listed in Table 1. These components were selected to be representative of current CubeSat subsystems and are not the same as those deployed on the Planet spacecraft.

Table 1. Sensor and actuator references.

Component	Model
GNSS receiver	Septentrio AsterRx4 <sup>36)</sup>
Thruster	Busek BET-100 <sup>37)</sup>
Reaction wheel	CubeWheel Medium <sup>38)</sup>

From the performance specifications of these components, the navigation and control performance is modeled as follows. It is assumed that the mothership's 1- $\sigma$  navigation errors are 5 m and 1 cm/s in position and velocity, respectively, after filtering. It is also assumed that the mothership is able to estimate the mean ROE of each deputy with 1- $\sigma$  uncertainty of 5 m and a bias of no more than 1 m using the differences in the position, velocity, and time measurements from the GNSS receivers. Finally, a 5% difference between the commanded and applied thrust is included in the simulations. These navigation and control errors are summarized in Table 2.

Table 2. Error parameters for simulations.

Error Source	Units	Value
Absolute Navigation		
Position (1- $\sigma$ )	(m)	5
Velocity (1- $\sigma$ )	(cm/s)	1
Relative Navigation		
Noise (1- $\sigma$ )	(m)	5
Bias	(m)	1
Maneuver Execution	(%)	5

For simulations using the low-thrust control law, each deputy is assigned a constant cross-section area of between 0.048 and 0.052 m<sup>2</sup>, resulting in differential ballistic coefficients of up to 0.0004 m<sup>2</sup>/kg, which is 4% of the ballistic coefficient of the mothership. Additionally, the BET-100 produces a thrust of 100  $\mu$ N, resulting in an acceleration of  $2.2 \times 10^{-5}$  m/s<sup>2</sup>.

For simulations using differential drag control, the commanded differential ballistic coefficients are cast as attitude commands as described in the following. If the axis of the CubeSat body is aligned in the radial direction (e.g. to orient the telescope in the nadir direction) and  $\beta$  denotes the angle between the solar panel array and the flight direction, then the cross-section area can be approximated as

$$A = 0.03 \cos(\beta) + 0.21 |\sin(\beta)| \quad (77)$$

From this function, the commanded values of  $\beta$  corresponding to minimum and maximum drag are set at 0 and 11.2 degrees, respectively, resulting in cross-section areas of 0.03 and 0.07 m<sup>2</sup>. These areas provide differential ballistic coefficients of 0.004 m<sup>2</sup>/kg, which is 40% of the ballistic coefficient of the mothership. The nominal attitude for each deputy is set between 5.0 and 6.1 degrees, providing nominal areas between 0.048 and 0.052 m<sup>2</sup> as in the simulations using the low-thrust control law. Since the attitude of the spacecraft cannot be changed instantaneously, the output of the bang-off-bang control law is used to drive a simple one-dimensional attitude controller. The attitude controller assumes a spacecraft moment of inertia  $I$  of 0.05 kgm<sup>2</sup>, a maximum torque of 0.001 Nm,<sup>38)</sup> and momentum storage of 0.01 Nms.<sup>38)</sup> These result in a maximum angular acceleration of 1.1 deg/s<sup>2</sup> and a maximum slew rate of 11 deg/s. The commanded torque  $P$  to the attitude controller is given as

$$P = I(-2\eta\dot{\beta} - \eta^2(\beta - \beta^{com})) \quad (78)$$

where  $\beta^{com}$  is the attitude command from the bang-off-bang control law and  $\eta$  is the parameter governing the convergence speed. This parameter is set at 0.05 in order to reduce the load on the reaction wheel. This control law produces a maximum torque command of only 27  $\mu$ Nm when the difference between the true and commanded attitude is 11.2°. Additionally, attitude command is only sampled once every five minutes to reduce the number of attitude slew maneuvers.

The initial orbit of the mothership is given in Table 3. This

Table 3. Initial mothership orbit.

$a$ (km)	$e$ (-)	$i$ (°)	$\Omega$ (°)	$\omega$ (°)	$M$ (°)
6,835	0.001	20	120	120	0

orbit was selected to provide a nominal altitude of 450 km. At this altitude the atmospheric density is sufficient to allow the differential drag control law to counteract the effects of solar radiation pressure and third-body gravity, but small enough to allow several days of free drift without the along track separation growing larger than a few kilometers. Given the described spacecraft models and initial orbit, the key parameters for the low-thrust and differential drag control laws are given in Table 4. The deadband values are selected to allow a control error five

Table 4. Control law parameters.

Controller	Low-thrust	Differential drag
$a\delta\lambda_{db}$ (m)	25	25
$a\delta e_{db}$ (m)	25	25
$\zeta$ (deg)	80	80
$U_{thrust}$ (m/s <sup>2</sup> )	$2.2 \times 10^{-5}$	N/A
$U^*$ (m/s <sup>2</sup> )	$1.0 \times 10^{-5}$	N/A
$\Delta t_{rec}$ (days)	2.25	N/A
$\Delta B_{max}$ (m <sup>2</sup> /kg)	N/A	0.02 (40% of $B_c$ )
$\Delta B^*$ (m <sup>2</sup> /kg)	N/A	0.0089 (18% of $B_c$ )
$\bar{\rho}$ (kg/m <sup>3</sup> )	N/A	$1.05 \times 10^{-12}$
$D$ (-)	N/A	4.5

times larger than the 1- $\sigma$  relative navigation error. The averaged density over the orbit is computed from the Harris-Priester atmospheric density model<sup>39)</sup> and is assumed constant for the entire simulation. The  $U^*$  and  $\Delta B^*$  parameters are computed from

Eqs. (51) and (69), respectively.  $D$  is computed by dividing  $\Delta B^*$  by the largest nominal differential ballistic coefficient of the deputies. The reconfiguration time for the low-thrust controller is selected to satisfy the constraint in Eq. (58) for the drift window described in the following. Finally, in order to assess the robustness of the differential drag control architecture to errors in atmospheric density models, simulations are also performed where the estimated  $\bar{\rho}$  is half or double the true value.

Next, it is necessary to select the initial configuration for the swarm formations. A nominal separation  $a\delta e_{sep}$  of 200 m is selected so that Eq. (21) is satisfied for any  $a\delta\lambda$  in the 25 m deadband. The deputies are arranged as in Eq. (18) and the initial relative eccentricity vector for each of the deputies with respect to the mothership is shown in Figure 15.

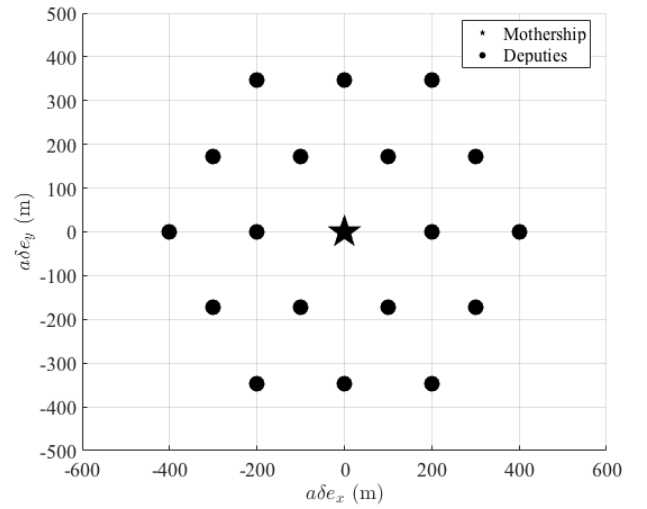


Fig. 15. Initial configuration of high-density swarm.

The nominal sizing for the formation using  $e/i$  vector separation is driven by the duration of the passive drift phase. If it is assumed that  $a\delta i$  drifts by no more than 25 meters over the simulation, then nominal separations  $a\delta e_{sep}$  and  $a\delta i_{sep}$  of 400 meters are sufficient to satisfy the constraint in Eq. (31) whenever  $\text{mod}(\theta, 180^\circ)$  is between  $45^\circ$  and  $135^\circ$ , allowing multiple days of passive drift. The initial configuration of this formation is illustrated in Figure 16. For simulations using low-thrust con-

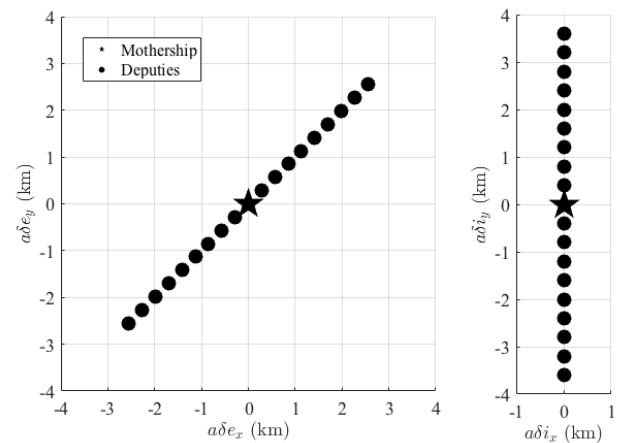


Fig. 16. Initial configuration swarm using  $e/i$  vector separation.

control, the formation is allowed to drift whenever  $\text{mod}(\theta, 180^\circ)$  is between  $45^\circ$  and  $105^\circ$ . These drift phases are 4.5 days in duration. The reconfiguration time specified in Table 4 ensures that  $\delta\lambda$  satisfies the constraint in Eq. (21) before  $\text{mod}(\theta, 180^\circ)$  exceeds  $135^\circ$ . For simulations using differential drag control, the reconfiguration time is expected to be equal to the drift time for a  $D$  of 4.5 according to Eq. (73). However, this will only be true if the controller closely follows the modeled trajectory, which requires an accurate estimate of the density. In order to allow some margin for error in the density estimate, the formation is allowed to drift whenever  $\text{mod}(\theta, 180^\circ)$  is between  $45^\circ$  and  $75^\circ$ . These windows are each 2.25 days in duration. This allows 4.5 days for the differential drag control law to recover safe relative motion in the RT-plane.

Each simulation is propagated for ten weeks (approximately 1000 orbits) using a high-fidelity numerical orbit propagator including all relevant perturbations affecting spacecraft in LEO.<sup>40)</sup> The perturbation models used by the propagator are included in Table 5. The computation sequence used to pro-

Table 5. Numerical orbit propagator parameters.

Integrator	Runge-Kutta (Dormand-Prince)
Step size	Fixed: 10 sec
Geopotential	GGM01S (20x20) <sup>41)</sup>
Atmospheric density	Harris-Priester <sup>39)</sup>
Third body gravity	Lunar and solar point masses, analytical ephemerides
Solar radiation pressure	Satellite cross-section normal to the sun, no eclipses

duce the ground truth mean ROE used to assess performance of the control architectures is shown in Figure 17 and described in the following. First, the absolute position and velocity  $\mathbf{x}$  of the mothership and all deputies are numerically integrated using the described propagator including the maneuvers performed by each deputy. These position and velocity trajectories are then converted into osculating orbits. Next, the osculating to mean transformation described by Schaub<sup>42)</sup> is applied to the osculating orbits in order to remove short-period oscillations due to  $J_2$ . These mean orbits are used to compute the ground truth mean ROE.

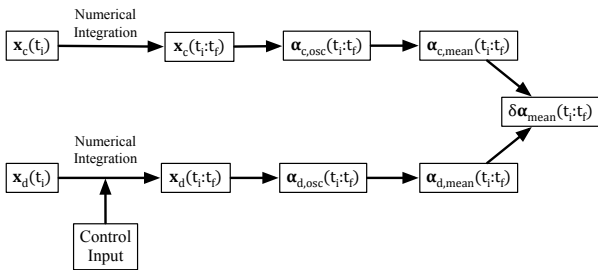


Fig. 17. Computation of ground truth reference.

The computation sequence used to compute the commanded actuation for each deputy is illustrated in Figure 18 and described in the following. At each time step, the estimated absolute position and velocity of the mothership is computed by adding the previously described absolute state error to the ground truth. This estimated state is converted to an osculating

orbit, which is then converted to a mean orbit using Schaub's osculating to mean transformation.<sup>42)</sup> The relative state estimate for each deputy is computed by adding the aforementioned relative state noise to the true mean ROE. These absolute and relative state estimates are used to compute the commanded actuation. For simulations using low-thrust control, the commanded acceleration is computed every ten seconds. For simulations using differential drag control, the commanded attitude is only computed once every five minutes in order to reduce load on the reaction wheel.

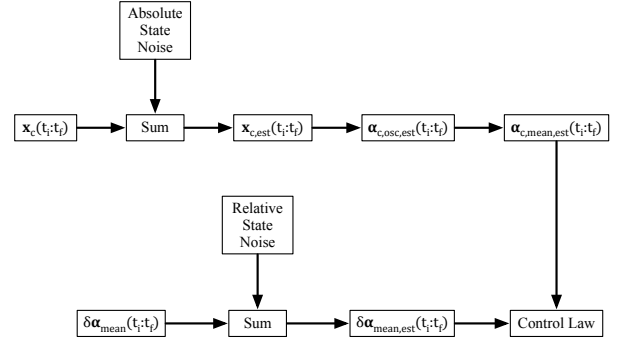


Fig. 18. Computation of state estimates and control command.

Using the equations derived in the previous sections, it is possible to produce an a-priori estimate of the delta-v costs associated with the low-thrust control simulations. In order to maintain equal orbit energies, the control law must at minimum negate the average relative acceleration due to differential drag. The delta-v cost can be estimated by multiplying the average acceleration computed from Eq. (65) and the simulation time. For a differential ballistic coefficient of  $0.0004 \text{ m}^2/\text{kg}$  (4% of  $B_c$ ) and  $\bar{\rho}$  taken from Table 4, this produces a delta-v lower bound of 7 cm/s for the entire ten week simulation. However, for simulations in which the swarm is allowed to drift, the control law will have to produce larger maneuvers in order to counteract the drift in  $\delta\lambda$ . From Eq. (59), the required maneuvers incur triple the delta-v cost of simply counteracting the change in  $\delta a$  over the drift phase for the specified control duty cycle. Since the drift and reconfiguration cycles span half of the simulation duration, the estimated minimum delta-v cost for these simulations is 14 cm/s. Finally, the drift and reconfiguration parameters can be estimated using Eqs. (53), (56), (71), and (72). These estimates are included in Table 6 for a nominal differential ballistic coefficient of 4% of  $B_c$ .

Table 6. Simulation drift and reconfiguration parameter estimates.

Low-Thrust Control	
$a\delta a_{drift}$ (m)	17
$a\delta\lambda_{drift}$ (km)	5.6
$a\delta a_{rec}$ (m)	17
Differential Drag Control	
$a\delta a_{drift}$ (m)	8.5
$a\delta\lambda_{drift}$ (km)	1.4
$a\delta a_{rec}$ (m)	14
$a\delta\lambda_{rec}$ (km)	1.7

## 6. Results

The performance of the formation designs and control architectures is assessed using the metrics described in the following. The first metric is the minimum separation  $\delta r$  between any two spacecraft in Cartesian space at any time during the simulation. The simulation is considered a success if the minimum separation is greater than the previously specified minimum safe separation of 125 m. The second performance metric is given by the total delta-v cost  $\Delta v$  for simulations using low-thrust control. The actuation cost for differential drag control is measured by two performance metrics. The first metric  $P_{max}$  denotes the largest torque commanded by any deputy over the complete simulation, which should be less than 1 mNm to satisfy the constraints of the CubeWheel Medium reaction wheel. The second metric  $P_{mean}$  denotes the largest mean torque, which is computed for each deputy by integrating the absolute value of  $P$  over the simulation and dividing by the total time. A high  $P_{max}/P_{mean}$  ratio indicates that the attitude controller is operating at a low duty cycle on all spacecraft. The final performance metrics are the maximum values of  $a|\delta a|$ ,  $a|\delta \lambda|$ , and  $a\|\delta \mathbf{e}_{err}\|_2$  during the simulation. For simulations of the high-density swarm formation, the largest values of  $a|\delta \lambda|$  and  $a\|\delta \mathbf{e}_{err}\|_2$  should not exceed the 25 m deadband value and the maximum value of  $a|\delta a|$  should be a few meters or less. For simulations of the swarm using e/i vector separation, the maximum values of  $a|\delta a|$  and  $a|\delta \lambda|$  are compared to the estimates in Table 6. The maximum value of  $a\|\delta \mathbf{e}_{err}\|_2$  is allowed to exceed the 25 m deadband during the drift, but should be small relative to  $a\delta e_{sep}$  to ensure sufficient separation in the RN-plane over the complete drift phase.

### 6.1. High Density Swarm

The performance metrics for the simulations of the high-density swarm formation using both low-thrust and differential drag control are given in Table 7. Both of these simulations have minimum separations of over 125 m, ensuring collision free relative motion for the entire swarm. Additionally, both controllers are able to ensure that  $\delta \lambda$  and  $\delta \mathbf{e}$  are within a few meters of their respective deadbands at all times. The maximum torque applied by any of the spacecraft is small relative to the capabilities of the CubeWheel Medium reaction wheel, demonstrating that the required actuation can be achieved with minimal agility requirements. Finally, the total delta-v cost for the low-thrust control law is within a factor of three of the predicted minimum delta-v cost.

To understand this difference, consider the evolution of the ROE for all of the deputies over two days of simulation shown in Figure 19. It can be seen that some of the deputies follow a limit cycle in  $\delta a$  and  $\delta \lambda$ . In order to follow this trajectory, the spacecraft must periodically perform equal and opposite maneuvers to reverse the residual drift in  $\delta \lambda$ . Specifically, since  $a\delta a$  is normally one meter or less, these maneuvers should have a delta-v cost on the order of 1 mm/s according to Eq. (32). The total delta-v cost of 19 cm/s is consistent with a single 1 mm/s maneuver performed once every five orbits. However, even with this limit cycle, the controller could be implemented for a year before the total delta-v cost per spacecraft exceeds 1 m/s. It can also be seen that the relative inclination vector drifts

Table 7. High-density swarm simulation performance metrics.

Low-Thrust Control		
$\min(\delta r)$	(m)	158
$\Delta v$	(cm/s)	19
$\max(a \delta a )$	(m)	4.6
$\max(a \delta \lambda )$	(m)	29
$\max(a\ \delta \mathbf{e}_{err}\ _2)$	(m)	29
Differential Drag Control		
$\min(\delta r)$	(m)	187
$P_{max}$	( $\mu$ Nm)	24
$P_{mean}$	( $\mu$ Nm)	0.65
$\max(a \delta a )$	(m)	1.6
$\max(a \delta \lambda )$	(m)	29
$\max(a\ \delta \mathbf{e}_{err}\ _2)$	(m)	23

very slowly over the simulation, validating the claim in Sec. 2 that it is constant under the effects of  $J_2$  and differential drag if  $\delta a$  and  $\delta i_x$  are zero. Finally, the relative eccentricity vectors closely follow the passive rotation due to  $J_2$ .

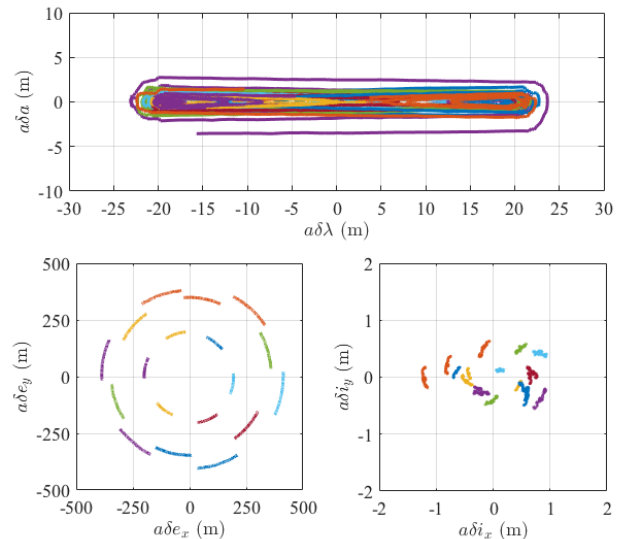


Fig. 19. ROE evolution over two days for high-density swarm using low-thrust control.

### 6.2. E/I Vector Separation Swarm

The performance metrics for the simulations of the swarm formation based on e/i vector separation using both low-thrust and differential drag control are given in Table 8. It is evident from these metrics that both simulations provide a minimum separation well over the 125 m requirement. Additionally, the actuation cost metrics for differential drag control are nearly identical to the metrics for the high-density swarm. It is noteworthy that the maximum error in the relative eccentricity vector is significantly larger than the maximum value of  $\delta a$ , which contradicts the expected behavior due to differential drag. This error likely derives from the fact that the guidance profile follows the rotation of the relative eccentricity vector defined in Eq. (3), which is linearized in separation. Because the largest nominal  $a\delta e$  for any of the deputies in this swarm is 3600 m, it is likely that this error derives from the higher-order separation effects of  $J_2$ . Nevertheless, even with an error of 105 m in the low-thrust control simulation, the spacecraft should have

a minimum separation of 190 m when the relative eccentricity vectors are vertical according to Eq. (31), which is close to the observed minimum separation of 211 m. Thus, it is clear that the control laws are robust to small unmodeled perturbations affecting  $\delta e$ .

Table 8. E/I vector separation swarm simulation performance metrics.

Low-Thrust Control		
$\min(\delta r)$	(m)	211
$\Delta v$	(cm/s)	64
$\max(a \delta a )$	(m)	36
$\max(a \delta \lambda )$	(m)	7.7
$\max(a\ \delta e_{err}\ _2)$	(m)	105
Differential Drag Control		
$\min(\delta r)$	(m)	280
$P_{max}$	( $\mu\text{Nm}$ )	24
$P_{mean}$	( $\mu\text{Nm}$ )	0.82
$\max(a \delta a )$	(m)	17
$\max(a \delta \lambda )$	(m)	2.8
$\max(a\ \delta e_{err}\ _2)$	(m)	50

Also, there are significant differences between the reconfiguration parameters and their predicted values. Additionally, the total delta-v cost is significantly larger than both the estimate from the duty cycle of the controller and the cost from the high-density swarm simulation. This is noteworthy because it is expected that the drift phases would reduce the number of maneuvers performed during the simulation, reducing the delta-v cost incurred by uncorrelated maneuver execution errors. In order to interpret these results, it is necessary to consider the transient behavior of  $\delta a$  and  $\delta \lambda$  during the drift and reconfiguration phases. The evolution of these state components during the low-thrust control simulation for the deputy with the largest differential ballistic coefficient is shown in Figure 20. In this figure, the top plot shows the behavior during the drift and reconfiguration phases and the lower plot shows a close-up of the behavior near the deadband. This plot exhibits two interesting properties. First, the path traced out by the deputy is qualitatively similar to the modeled path shown in Figure 11, validating the modeling assumptions. Second, the maximum value of  $\delta \lambda$  for each of the free drift phase varies by up to 30%. This suggests that the mean density over the orbit is changing over the simulation due to the precession of the orbit due to  $J_2$  and the effect of solar motion on the diurnal bulge.

This plot can also be used to explain the differences between the predicted and observed performance metrics. First, because  $a\delta a$  is between 10 and 20 m at the end of the drift phases (parabolas at the bottom of the plot), the model described in Eq. (56) suggests that the value of  $a\delta a$  after the first maneuver should be 10 to 20 meters, but the simulation shows values of 20 to 30 meters. This difference is caused by the navigation errors in the state estimates used to compute the commanded acceleration. Specifically, when  $a\delta a$  is within 5 m of the switching line of the control law, the navigation errors will occasionally produce state estimates that result in a commanded maneuver. However, when  $a\delta a$  is at least 10 m from the switching line, these events become very rare. This 10 m overshoot in the maneuver is consistent with the observed results. Additionally, recall that the total delta-v cost is proportional to the change in  $\delta a$

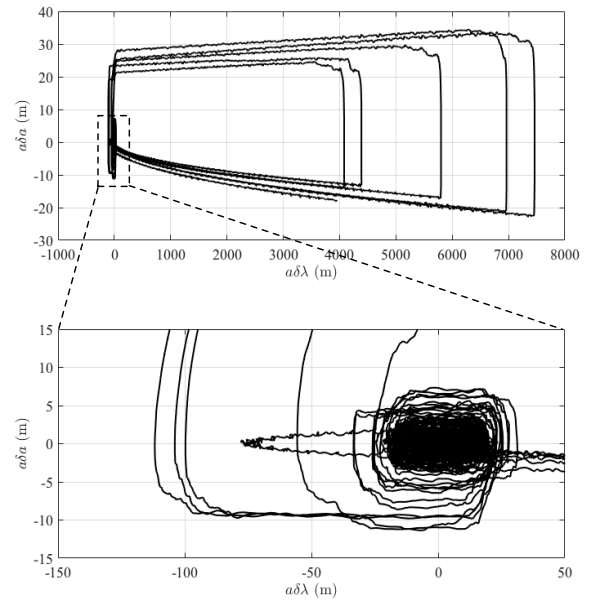


Fig. 20. State space trajectory of  $\delta a$  and  $\delta \lambda$  using low-thrust control.

produced by the maneuvers. As a result of the increased maneuver size due to the relative navigation errors, the change in  $a\delta a$  produced by the reconfiguration maneuvers over the simulation (length of the vertical lines in the top plot) is larger than 500 m, which corresponds to a delta-v cost of 25 cm/s according to Eq. (32). This is already larger than the total delta-v cost from the high-density swarm simulation. Also, it can be seen from the close-up plot that the control law has a tendency to overshoot the deadband by up to 100 m, then spiral towards the origin. This overshoot can be attributed to the modulation produced by the control law for the relative eccentricity vector. Specifically, after a deputy crosses the switching line, it may have to wait up to half an orbit before a maneuver can be performed with a favorable effect on  $\delta e$ . From the relationship between  $\delta a$  and the drift rate of  $\delta \lambda$  in Eq. (34), this spiraling behavior requires a maneuver to be performed nearly every orbit until  $\delta a$  and  $\delta \lambda$  reach the steady-state limit cycle shown in Figure 19. It follows that the number of maneuvers performed in this simulation is actually larger than the number of maneuvers in the high-density swarm simulation. Additionally, the change in  $a\delta a$  produced by these maneuvers is several times larger than that of the maneuvers in the steady-state limit cycle, so the remaining delta-v cost can be attributed to the maneuvers performed during this spiraling phase. Overall, the increased delta-v cost can be attributed to the effect of navigation errors on the reconfiguration maneuvers and the subsequent maneuvers required to stabilize  $\delta a$  and  $\delta \lambda$  within the deadband. However, the total costs are still much less than 1 m/s per month for all spacecraft in the swarm. The Busek BET-100 thruster has a delta-v capacity of 40 m/s for a 4.5 kg CubeSat, allowing this control architecture to be used for several years.

It is also interesting to consider the evolution of  $\delta a$  and  $\delta \lambda$  over time. These components are plotted with respect to  $\theta$  in Figure 21. Because the drift and control periods are periodic,  $\theta$  serves as an analog for time because the relative eccentricity

vectors of all deputies rotate due at the same rate due to  $J_2$ . Furthermore, the equations that govern the minimum separation in the RN-plane (Eqs. (10) and (31)) are explicit functions of  $\theta$ . In particular the x-axis on this plot takes the modulus of  $\theta$  and  $180^\circ$  to allow the drift and reconfiguration phases to be directly overlaid. In the red region, the minimum RN-plane separation is known to be less than 125 m according to Eq. (10), requiring the control law to ensure separation in the RT-plane. In the orange region it is possible that adjacent spacecraft may have insufficient RN-plane separation according to Eq.(31) if their respective positions in the deadband are poor. Outside of these regions, the minimum RN-plane separation is guaranteed to be at least 125 m. The green region indicates the drift phase of the swarm and the reconfiguration phase occurs in the white region. It can be seen that the control law is able to constrain  $\delta\lambda$  to within the deadband well in advance of when the RN-plane separation constraint is violated. This is largely caused by the increased maneuver size due to the relative navigation errors. The increased relative semimajor axis causes  $\delta\lambda$  to drift back to the deadband faster than predicted. Additionally, it can be seen that the rate of change of  $\delta a$  during the drift periods varies over the simulation. Since the ballistic coefficient of the spacecraft is constant and the change in the semimajor axis over the simulation is small, this variation must be due to changes in the atmospheric density.

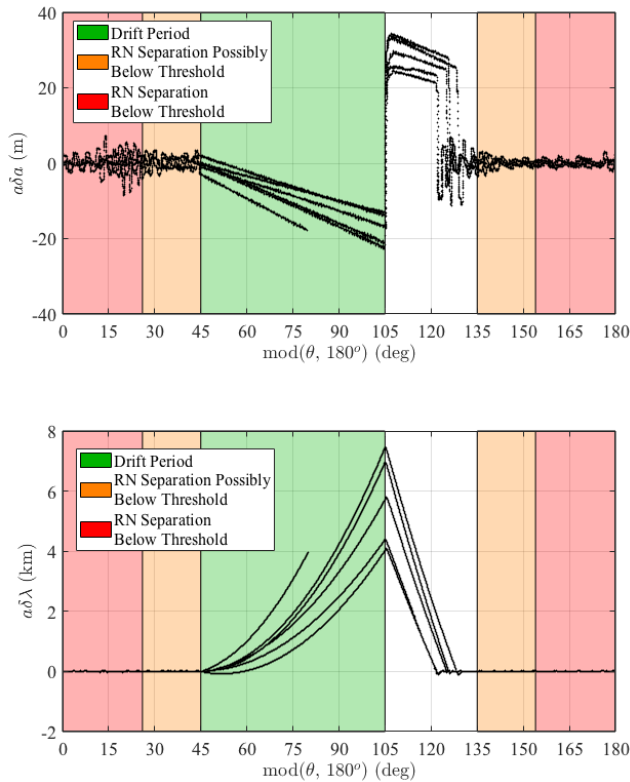


Fig. 21. Evolution of  $\delta a$  (top) and  $\delta\lambda$  (bottom) vs  $\theta$  for low-thrust control.

Next, consider the trajectory followed by  $\delta a$  and  $\delta\lambda$  for the deputy with the largest differential ballistic coefficient during the differential drag control simulation as shown in Figure 22. The shape of the trajectory over the drift and reconfiguration phases is similar to that shown in Figure 13. Additionally, the

drift and reconfiguration cycles have different sizes due to the varying atmospheric density over the simulation.

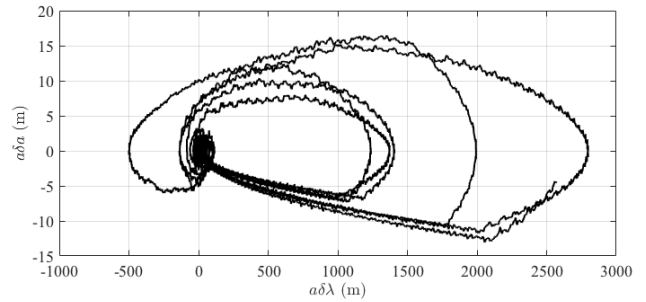


Fig. 22. State space trajectory of  $\delta a$  and  $\delta\lambda$  using differential drag control.

To characterize the transient performance of the controller, these components are plotted against  $\theta$  in Figure 23. Recall that a change in  $\theta$  of  $30^\circ$  corresponds to an elapsed time of 2.25 days. Additionally, according to Eq. (73) the reconfiguration time should be equal to the drift time for a  $D$  of 4.5. However, it can be seen in Figure 23 that the control law only reliably converges before  $\theta$  is approximately  $120^\circ$ . At this point, the control law has been engaged for 3.4 days. This difference can be attributed to both the varying density over the simulation and variations in the density over a single orbit due to the diurnal bulge. Specifically, if the control law for the relative eccentricity vector only allows maneuvers to be performed in a region of low density, differential drag maneuvers will not be as effective as predicted. This can cause an increase in the reconfiguration time.

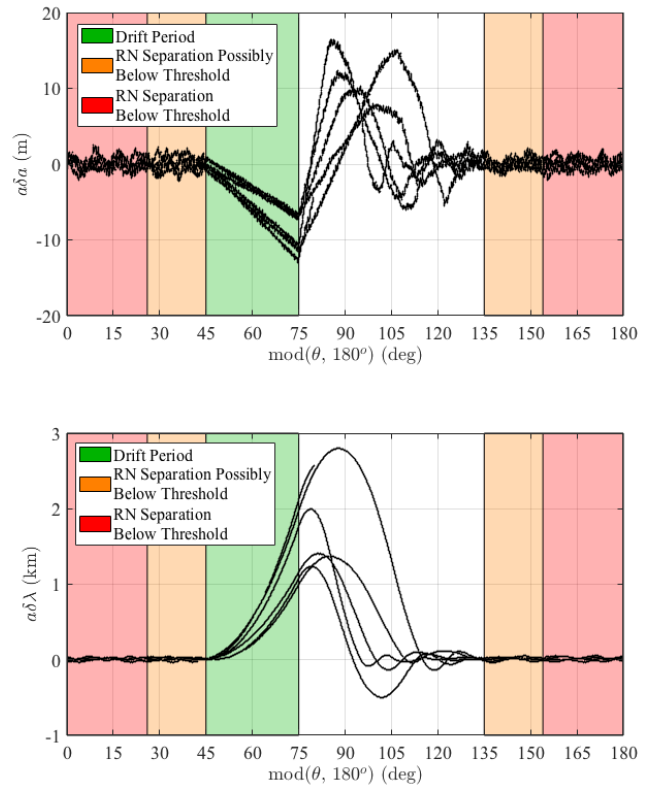


Fig. 23. Evolution of  $\delta a$  (top) and  $\delta\lambda$  (bottom) vs  $\theta$  for differential drag control.

The simulations for the differential drag control law were repeated using density estimates of half and double the value specified in Table 4. Both of these simulations have minimum inter-spacecraft separations of 280 m. The remainder of the performance metrics are not significantly different from those of the nominal case. The main differences in these simulations appears in the transient behavior of  $\delta a$  and  $\delta \lambda$ . First, consider the plots of  $\delta a$  and  $\delta \lambda$  for the simulation with underestimated density shown in Figure 24. There are three main differences between these plots and those in Figure 23: 1) the maximum value of  $\delta a$  during the reconfiguration is slightly reduced, 2) the time required to reach zero  $\delta \lambda$  is increased, and 3) overshoot in  $\delta \lambda$  is nearly eliminated. These effects can be interpreted as follows. Because the control law underestimates the density, maneuvers are often more effective than predicted. Additionally, the switching line for the control law will constrain  $\delta a$  to smaller values. As a result, the trajectory will remain close to the switching line shown in Figure 12 and will not overshoot the deadband.

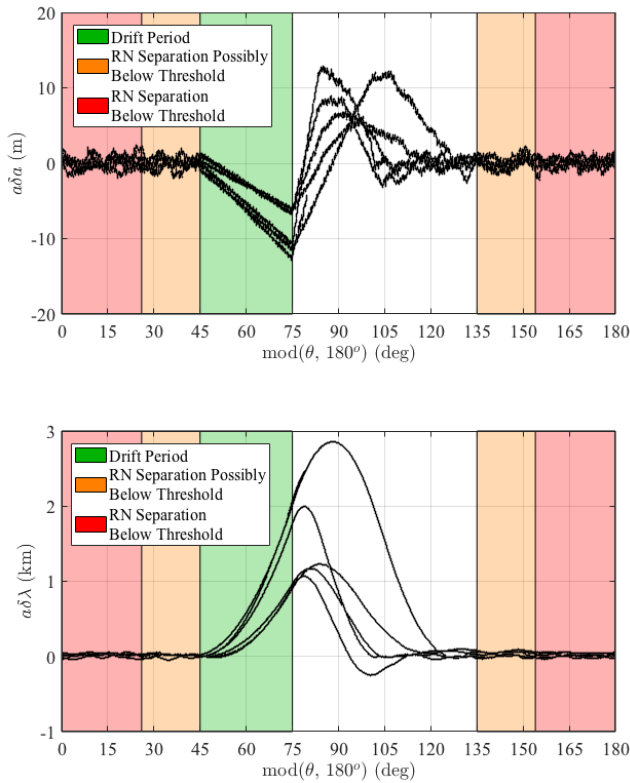


Fig. 24. Evolution of  $\delta a$  (top) and  $\delta \lambda$  (bottom) vs  $\theta$  for differential drag control with underestimated density.

Next, consider the plots of  $\delta a$  and  $\delta \lambda$  for the simulation with overestimated density shown in Figure 25. There are two main differences between these plots and those in Figure 23: 1) the maximum value of  $\delta a$  during the reconfiguration is increased, and 2) the controller always overshoots the deadband, resulting in an increased convergence time. These behaviors can be interpreted as follows. Because the controller overestimates the density, maneuvers are often less effective than expected. Additionally, the switching line for the control law allows for larger values of  $\delta a$  closer to the deadband. As a result, the controller is unable to follow the switching line and regularly overshoots

the deadband, requiring multiple maneuver cycles to converge. However, the controller is able to converge to the deadband before the conservative RN-plane separation condition is violated in all of these simulations. It is therefore clear that selecting a conservative reconfiguration time for the hybrid passive/active control architecture provides robustness to atmospheric density modeling errors.

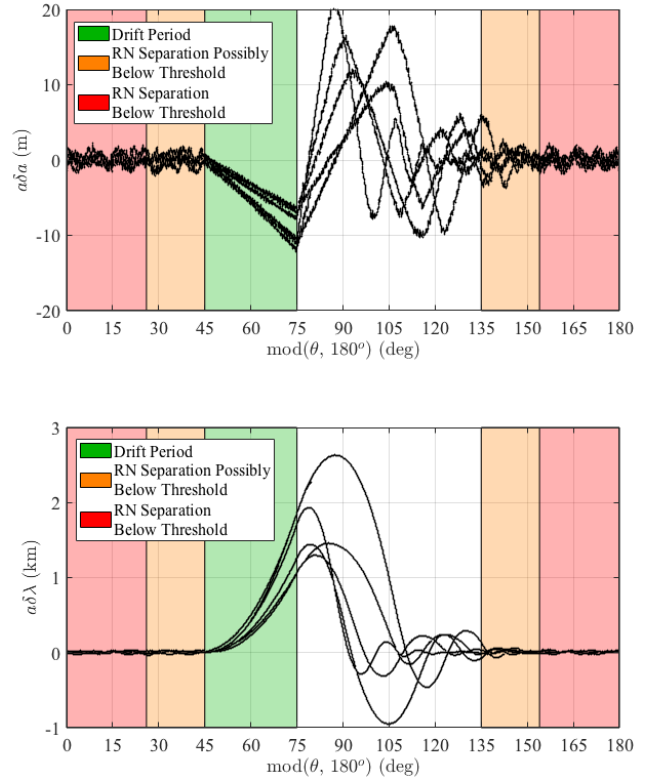


Fig. 25. Evolution of  $\delta a$  (top) and  $\delta \lambda$  (bottom) vs  $\theta$  for differential drag control with overestimated density.

Overall, these results show that the proposed swarm designs are able to provide safe and bounded relative motion to swarms of tens of spacecraft for weeks or longer with minimal actuation. Additionally, the actuation requirements can be met with either low-thrust or differential drag control. The delta-v costs associated with the low-thrust controller are low enough to allow such a swarm to operate for years in LEO using current COTS CubeSat thrusters. Furthermore, the ability to use differential drag control suggest that a swarm mission could be deployed on spacecraft that are only equipped with attitude control, dramatically reducing mission costs and allowing extremely long mission lifetimes.

## 7. Conclusion

Future missions using spacecraft swarms will require guidance and control systems that are more efficient with respect to computation and propellant costs than those currently available in literature. To meet this need, this paper presents a new guidance and control methodology for spacecraft swarms based on relative orbital elements. The main contribution of this paper is a means of generalizing the flight-proven techniques used to design and control binary formations to accom-

modate a large number of spacecraft. Using this approach, formation designs and control architectures are found that ensure safe and bounded relative motion of a swarm in orbits perturbed by both  $J_2$  and differential drag at minimum actuation and computation cost. In particular, linear constraints that ensure passively bounded relative motion in  $J_2$ -perturbed near-circular orbits are derived from a recently derived state transition matrix for spacecraft relative motion. Additionally, a formation design is found that generalizes the eccentricity/inclination vector separation concept to an arbitrary number of spacecraft. This formation ensures passively safe relative motion for multiple days under the effects of both  $J_2$  and differential drag. Furthermore, a technique for ensuring collision avoidance between all spacecraft in a swarm including uncertainty at low computational cost is presented. Finally, efficient control laws are derived that can be implemented using low-thrust or differential drag control.

The performance of these formation designs and control architectures is validated through implementation in a simulated mission scenario. These simulations demonstrate that all of the proposed designs are able to provide safe and bounded relative motion to a large number of spacecraft in close proximity at minimal actuation and computation cost. In particular, the delta-v cost per spacecraft of using the low-thrust control law is only 19 cm/s for a ten week simulation at an altitude of 450 kilometers. Additionally, allowing periodic drifts covering one third of the simulation time for the formation based on eccentricity/inclination vector separation results in a delta-v cost of 65 cm/s. The increased delta-v cost is due to the effect of relative navigation errors on the reconfiguration maneuvers and a set of additional maneuvers that is required to stabilize the state within the deadband of the control law. Nevertheless, these costs suggest that mission lifetimes of years are feasible using current commercially available thrusters for CubeSats. Additionally, simulations using differential drag control show that it is possible to control a swarm of spacecraft equipped with only attitude actuators. Such a swarm would reduce costs as compared to swarm designs that require thrusters and allow longer mission lifetimes

However, the models presented in this paper are subject to three main limitations. First, only the  $J_2$  and differential drag perturbations are considered, so these models are only applicable to swarms in low earth orbit. Second, the employed dynamics model uses an approximation of the secular and long-period effects of  $J_2$  that is linearized in separation. As a consequence, the specified guidance profile deviates from the observed passive relative motion at separations on the order of kilometers. While simulation results show that the control law is able to correct for this difference, a more sophisticated guidance profile may be required for swarms spanning a larger area. Third, the analytical constraints derived in this paper are only valid for near circular orbits. Future works will apply these techniques to eccentric orbits and include other perturbations, allowing safe and efficient operation of spacecraft swarms in a wide range of orbit regimes.

## Acknowledgments

This work was supported by a NASA Office of the Chief Technologists Space Technology Research Fellowship (NSTRF), NASA Grant #NNX15AP70H and the King Abdulaziz City for Science and Technology (KACST).

## References

- 1) B. D. Tapley, S. Bettadpur, M. Watkins, and C. Reigber, "The gravity recovery and climate experiment: Mission overview and early results," *Geophysical Research Letters*, Vol. 31, No. 9, 2004, DOI: 10.1029/2004GL019920.
- 2) G. Krieger, A. Moreira, H. Fiedler, I. Hajnsek, M. Werner, M. Younis, and M. Zink, "TanDEM-X: A Satellite Formation for High-Resolution SAR Interferometry," *IEEE Transactions on Geoscience and Remote Sensing*, Vol. 45, No. 11, 2007, pp. 3317–3341, DOI: 10.1109/TGRS.2007.900693.
- 3) J. L. Burch, T. E. Moore, R. B. Torbert, and B. L. Giles, "Magnetospheric Multiscale Overview and Science Objectives," *Space Science Reviews*, Vol. 199, No. 1, 2016, pp. 5–21, DOI: 10.1007/s11214-015-0164-9.
- 4) H. Schaub and K. T. Alfriend, " $J_2$  Invariant Relative Orbits for Spacecraft Formations," *Celestial Mechanics and Dynamical Astronomy*, Vol. 79, No. 2, 2001, pp. 77–95, DOI: 10.1023/A:1011161811472.
- 5) S. D'Amico, *Autonomous Formation Flying in Low Earth Orbit*. TU Delft, Delft University of Technology, 2010.
- 6) S. D'Amico and O. Montenbruck, "Proximity Operations of Formation-Flying Spacecraft Using an Eccentricity/Inclination Vector Separation," *Journal of Guidance, Control, and Dynamics*, Vol. 29, No. 3, 2006, pp. 554–563, DOI: 10.2514/1.15114.
- 7) D. P. Scharf, F. Y. Hadaegh, and S. R. Ploen, "A Survey of Spacecraft Formation Flying Guidance and Control (Part I): Guidance," *Proceedings of the 2003 American Control Conference, Denver, CO, June 4-6, Vol. 2*, 2003, pp. 1733–1739, DOI: 10.1109/ACC.2003.1239845.
- 8) D. P. Scharf, F. Y. Hadaegh, and S. R. Ploen, "A Survey of Spacecraft Formation Flying Guidance and Control (Part II): Control," *Proceedings of the 2004 American Control Conference, Boston, MA, June 30 - July 2, Vol. 4*, 2004, pp. 2976–2985.
- 9) H. Schaub, S. R. Vadali, J. L. Junkins, and K. T. Alfriend, "Spacecraft Formation Flying Control using Mean Orbit Elements," *Journal of the Astronautical Sciences*, Vol. 48, No. 1, 2000, pp. 69–87.
- 10) K. T. Alfriend and H. Yan, "Evaluation and Comparison of Relative Motion Theories," *Journal of Guidance, Control, and Dynamics*, Vol. 28, No. 2, 2005, pp. 254–261, DOI: 10.2514/1.6691.
- 11) K. T. Alfriend, S. R. Vadali, P. Gurfil, J. How, and L. Breger, *Spacecraft Formation Flying: Dynamics, control and navigation*. Butterworth-Heinemann, 2009.
- 12) J. Sullivan, S. Grimberg, and S. D'Amico, "A Comprehensive Survey and Assessment of Spacecraft Relative Motion Dynamics Models," *Journal of Guidance, Control, and Dynamics*, 2017, DOI: 10.2514/1.G002309.
- 13) P. K. C. Wang, "Navigation Strategies for Multiple Autonomous Mobile Robots Moving in Formation," *Journal of Field Robotics*, Vol. 8, No. 2, 1991, pp. 177–195, DOI: 10.1002/rob.4620080204.
- 14) W. Ren, R. W. Beard, and E. M. Atkins, "A Survey of Consensus Problems in Multi-Agent Coordination," *Proceedings of the 2005 American Control Conference, Portland, OR, June 8-10, 2005*, pp. 1859–1864, DOI: 10.1109/ACC.2005.1470239.
- 15) M. A. Hsieh, V. Kumar, and L. Chaimowicz, "Decentralized Controllers for Shape generation with Robotic Swarms," *Robotica*, Vol. 26, No. 05, 2008, pp. 691–701, DOI: 10.1017/S0263574708004323.
- 16) C. C. Cheah, S. P. Hou, and J. J. E. Slotine, "Region-Based Shape Control for a Swarm of Robots," *Automatica*, Vol. 45, No. 10, 2009, pp. 2406–2411, DOI: 10.1016/j.automatica.2009.06.026.
- 17) J. Alonso-Mora, A. Breitenmoser, M. Rufli, R. Siegwart, and P. Beardsley, "Image and Animation Display with Multiple Mobile

- Robots,” *The International Journal of Robotics Research*, Vol. 31, No. 6, 2012, pp. 753–773, DOI: 10.1177/0278364912442095.
- 18) M. E. Campbell, “Planning Algorithm for Multiple Satellite Clusters,” *Journal of Guidance, Control, and Dynamics*, Vol. 26, No. 5, 2003, pp. 770–780, DOI: 10.2514/2.5111.
  - 19) M. E. Campbell, “Collision Monitoring within Satellite Clusters,” *IEEE Transactions on Control Systems Technology*, Vol. 13, No. 1, 2005, pp. 42–55, DOI: 10.1109/TCST.2004.838550.
  - 20) S.-J. Chung and F. Y. Hadaegh, “Swarms of Femtosats for Synthetic Aperture Applications,” *Proceedings of the Fourth International Conference on Spacecraft Formation Flying Missions & Technologies, St. Hubert, Quebec, May 18-20, 2011*.
  - 21) S. Bandyopadhyay, S.-J. Chung, and F. Y. Hadaegh, “Probabilistic and Distributed Control of a Large-Scale Swarm of Autonomous Agents,” *IEEE Transactions on Robotics*, 2016. Submitted.
  - 22) D. Morgan, S.-J. Chung, L. Blackmore, B. Acikmese, D. Bayard, and F. Y. Hadaegh, “Swarm-Keeping Strategies for Spacecraft Under  $J_2$  and Atmospheric Drag Perturbations,” *Journal of Guidance, Control, and Dynamics*, Vol. 35, No. 5, 2012, pp. 1492–1506, DOI: 10.2514/1.55705.
  - 23) D. Morgan, *Guidance and Control of Swarms of Spacecraft*. PhD thesis, University of Illinois at Urbana-Champaign, 2015.
  - 24) D. Morgan, G. P. Subramanian, S.-J. Chung, and F. Y. Hadaegh, “Swarm Assignment and Trajectory Optimization using Variable-Swarm, Distributed Auction Assignment and Sequential Convex Programming,” *The International Journal of Robotics Research*, Vol. 35, No. 10, 2016, pp. 1261–1285, DOI: 10.1177/0278364916632065.
  - 25) O. Montenbruck, M. Kirschner, S. D’Amico, and S. Bettadpur, “E/I-vector separation for safe switching of the GRACE formation,” *Aerospace Science and Technology*, Vol. 10, No. 7, 2006, pp. 628–635, DOI: 10.1016/j.ast.2006.04.001.
  - 26) O. Montenbruck, R. Kahle, S. D’Amico, and J.-S. Ardaens, “Navigation and control of the TanDEM-X formation,” *The Journal of the Astronautical Sciences*, Vol. 56, No. 3, 2008, pp. 341–357, DOI: 10.1007/BF03256557.
  - 27) S. D’Amico, J.-S. Ardaens, and R. Larsson, “Spaceborne Autonomous Formation-Flying Experiment on the PRISMA Mission,” *Journal of Guidance, Control, and Dynamics*, Vol. 35, No. 3, 2012, pp. 834–850, DOI: 10.2514/1.55638.
  - 28) G. Gaias and S. D’Amico, “Impulsive Maneuvers for Formation Reconfiguration Using Relative Orbital Elements,” *Journal of Guidance, Control, and Dynamics*, Vol. 38, No. 6, 2014, pp. 1036–1049, DOI: 10.2514/1.G000189.
  - 29) M. Chernick and S. D’Amico, “New Closed-Form Solutions for Optimal Impulsive Control of Spacecraft Relative Motion,” *AIAA/AAS Astrodynamics Specialist Conference, Long Beach, California, September 13-16, 2016*.
  - 30) T. Guffanti, S. D’Amico, and M. Lavagna, “Long-Term Analytical Propagation of Satellite Relative Motion in Perturbed Orbits,” *27th AAS/AIAA Space Flight Mechanics Meeting, San Antonio, TX, February 5-9, 2017*.
  - 31) A. W. Koenig, T. Guffanti, and S. D’Amico, “New State Transition Matrices for Spacecraft Relative Motion in Perturbed Orbits,” *Journal of Guidance, Control, and Dynamics*, 2017, DOI: 10.2514/1.G002409.
  - 32) G. Gaias, J.-S. Ardaens, and O. Montenbruck, “Model of  $J_2$  perturbed satellite relative motion with time-varying differential drag,” *Celestial Mechanics and Dynamical Astronomy*, Vol. 123, No. 4, 2015, pp. 411–433.
  - 33) S. D’Amico, “Relative Orbital Elements as Integration Constants of the Hills Equations,” *DLR, TN 05-08, 2005*.
  - 34) F. d. Bruijn, E. Gill, and J. How, “Comparative Analysis of Cartesian and Curvilinear Clohessy-Wiltshire equations,” *Journal of Aerospace Engineering, Sciences and Applications*, Vol. 3, No. 2, 2011, pp. 1–15.
  - 35) C. Foster, H. Hallam, and J. Mason, “Orbit Determination and Differential-drag Control of Planet Labs Cubesat Constellations,” *AAS/AIAA Astrodynamics Specialist Conference, Vail, CO, August 9-13, 2015*.
  - 36) E. v. Rees, “Septentrio Satellite Navigation,” *GeoInformatics*, Vol. 18, No. 4, 2015, p. 10.
  - 37) B. C. Inc., “Busek BET-100 Datasheet,” URL: <http://www.busek.com/index.htm.files/70008516F.pdf>.
  - 38) S. U. Electronic Systems Laboratory, “CubeWheel Datasheet,” URL: <https://www.cubesatshop.com/wp-content/uploads/2016/06/CubeWheel-Option-Sheet-v1.2.pdf>.
  - 39) O. Montenbruck and E. Gill, *Satellite orbits: Models, Methods and Applications*. Springer Science & Business Media, 2012.
  - 40) D. Eddy, V. Giraldo, and S. D’Amico, “Development and Verification of the Stanford GNSS Navigation Testbed for Spacecraft Formation-Flying,” *9th International Workshop on Satellite Constellations and Formation Flight (IWSCFF), Boulder, CO, June 19-21, 2017*. Accepted.
  - 41) B. D. Tapley, F. Flechtner, S. V. Bettadpur, and M. M. Watkins, “The status and future prospect for GRACE after the first decade,” *AGU Fall Meeting Abstracts*, Vol. 1, 2013, p. 01.
  - 42) H. Schaub and J. L. Junkins, *Analytical Mechanics of Space Systems*. AIAA, 2003.